eChem
https://www.sciltp.com/journals/eChem

Review

Progress and Perspectives on NiFe Layered Double Hydroxide Catalysts for the Alkaline Oxygen Evolution Reaction

Zexuan Zheng [1], Liming Deng [2,*], Gengyu Xing [2], Shengjie Peng [3,4], Shaowei Chen [5], and Chade Lv [1,*]

[1] MIIT Key Laboratory of Critical Materials Technology for New Energy Conversion and Storage, State Key Laboratory of Space Power-Sources, School of Chemistry and Chemical Engineering, Harbin Institute of Technology, Harbin 150001, China
[2] College of Materials Science and Technology, Nanjing University of Aeronautics and Astronautics, Nanjing 210016, China
[3] Confucius Energy Storage Lab, School of Energy and Environment & Z Energy Storage Center, Southeast University, Nanjing 211189, China
[4] Shaoxing Research Institute of Renewable Energy and Molecular Engineering, Shanghai Jiao Tong University, Shaoxing 312000, China
[5] Department of Chemistry and Biochemistry, University of California, Santa Cruz, CA 95064, USA
* Correspondence: limingdeng@nuaa.edu.cn (L.D.); lv.chade@hit.edu.cn (C.L.)

How To Cite: Zheng, Z.; Deng, L.; Xing, G.; et al. Progress and Perspectives on NiFe Layered Double Hydroxide Catalysts for Alkaline Oxygen Evolution Reaction. *eChem* **2025**, *1* (1), 3. https://doi.org/10.53941/echem.2025.100003.

Received: 17 September 2025
Revised: 16 October 2025
Accepted: 16 October 2025
Published: 28 October 2025

Abstract: Anion exchange membrane water electrolysis (AEMWE) holds promise for low-cost hydrogen production, thereby addressing the energy crisis humanity faces. Of the two half-reactions, the hydrogen evolution reaction (HER) and the oxygen evolution reaction (OER), the latter, with sluggish dynamics, is the crucial one toward electrocatalytic water splitting, which requires a non-noble metal catalyst possessing high performance to make the reaction process efficient and economical. Such a condition requires a proper understanding of the reaction mechanism, careful design and optimization of catalyst materials, and maintenance of catalyst durability under AEMWE conditions during long-term operation. NiFe layered double hydroxide (NiFe-LDH), with its unique chemistry and electronic structure that facilitates moderate intermediate adsorption energies and offers tolerance to site deactivation, is of considerable interest as an electrocatalyst. In this review, we systematically discuss the OER catalytic mechanism in alkaline water electrolysis and provide evaluative criteria of the catalytic performance. Also, we summarize the corresponding synthesis strategies and characterization methods for NiFe-LDH catalysts, including morphology control, elemental doping, interfacial engineering, and defect construction. Furthermore, we address the recent bottleneck in developing NiFe-LDH catalysts for the OER under alkaline conditions and their application in AEMWE. Unlike previous reviews that separately discussed OER electrocatalysts or AEMWE operation, this work uniquely bridges the fundamental design of NiFe-LDH catalysts with their integration and performance in practical anion exchange membrane water electrolyzer systems. Finally, we share our thoughts regarding future development directions of NiFe-LDH catalysts toward alkaline OER, a critical step towards the commercialization of water electrolysis technology for green hydrogen production.

Keywords: NiFe layered double hydroxide; electrocatalysis; water splitting; oxygen evolution reaction; anion exchange membrane water electrolyzer

1. Introduction

Hydrogen possesses a high energy density and has played a pivotal role in addressing the issues of increasing energy demands and environmental crises. The global hydrogen production has exceeded 70 million metric tons (MMTs) per year, with the produced hydrogen consumed by metal refineries, the oil and gas industry, or converted into feedstock chemicals (e.g., CH_3OH), value-added products (e.g., NH_3), and other specialty chemicals [1]. In fact, hydrogen is also an effective energy source that contributes well to decarbonization and carbon neutrality [2,3]. Among the hydrogen production methods, green hydrogen production through water electrolysis has been attracting particular attention [4,5], which features an efficiency of 40–70% and high purity (>99%) of hydrogen production. Furthermore, in comparison to the widely used hydrocarbon refining technology that often releases significant amounts of greenhouse gases and pollutants, water electrolysis entails significantly reduced emissions of such harmful gases, especially when the electrolyzer is seamlessly integrated with renewable energy sources like solar panels and wind turbines [6].

The integration of advanced water electrolysis technologies, namely proton exchange membrane water electrolysis (PEMWE), alkaline water electrolysis (AWE), anion exchange membrane water electrolysis (AEMWE), and solid oxide electrolysis cells (SOEC), is central to the large-scale production of green hydrogen, especially when paired with low-carbon power sources such as renewables and nuclear-generated steam [7]. Among these technologies, SOEC stands out for its exceptionally high energy efficiency due to its operation at elevated temperatures ranging from 600–1000 °C. Under these conditions, a significant portion of the required energy is supplied thermally, reducing the electrical energy demand and enabling near-reversible water splitting. However, the harsh thermal environment imposes serious engineering and materials challenges, including thermal cycling stress, sealing complexity, and severe degradation of ceramic components, which collectively hinder SOEC’s long-term operational stability and commercial deployment [8]. These pathways highlight the trade-offs among efficiency, cost, and durability: SOECs maximize the thermal efficiency, PEMWE combine the compact design with the dependence on platinum group metals (PGMs), and AWE offer low cost but limited dynamics and stability. On the other hand, PEMWE systems operate under acidic conditions using a solid polymer electrolyte and rely on highly active precious metal electrocatalysts—iridium or ruthenium dioxide (RuO_2) at the anode and platinum (Pt) at the cathode. These systems offer compact cell design, rapid response times, and the ability to produce high-purity hydrogen at high current densities. However, their reliance on scarce and expensive PGMs raises concerns over cost and scalability [9–12]. In contrast, AWE uses non-precious, transition-metal-based electrocatalysts in a liquid electrolyte, typically 20–30 wt% KOH, and benefits from decades of operational maturity and low material costs [13]. While effective, AWE systems suffer from slow dynamic response and durability issues induced by the corrosive alkaline environment—problems that compromise the stability of catalysts and other components over long-term operation [13,14].

The AEMWE bridges the gap between PEMWE and AWE, combining the cost-effective, PGM-free catalyst strategy of AWE with the compact architecture and high-efficiency characteristics of PEMWE [11,14–17]. Operating under mildly alkaline conditions (≤1 M KOH), AEMWE allows the use of non-noble metal catalysts while reducing material degradation associated with the harsher environments of both AWE and PEMWE. Moreover, AEMWE can achieve higher current densities than traditional AWE, without relying on expensive PGMs, making it a strong candidate for affordable, scalable hydrogen production [18]. However, a significant bottleneck remains in the OER at the anode. The OER under alkaline conditions is characterized by inherently sluggish kinetics, requiring high overpotentials to sustain industrial-scale current densities [19–21]. This not only reduces system efficiency but also accelerates the degradation of the membrane, ionomer, and electrocatalyst materials. Membranes are particularly prone to chemical degradation under high pH and oxidative conditions, while transition-metal-based catalysts may suffer from phase changes, dissolution, or passivation [22]. Additionally, ensuring robust interfacial contact and ionic conductivity between the membrane, catalyst layers, and ionomers is critical to maintain long-term performance [21,22]. Addressing these challenges requires continued development of durable, chemically stable anion exchange membranes and highly active, corrosion-resistant PGM-free OER catalysts. Until these performance and lifetime limitations are overcome, AEMWE, despite its substantial promise, will remain in the early stages of commercial adoption compared to its more mature counterparts.

In this review, we systematically analyze the recent progress of NiFe layered double hydroxides (NiFe-LDHs) as oxygen evolution reaction (OER) electrocatalysts for application in anion-exchange-membrane water electrolyzers (AEMWEs). The study of Fe-containing layered double hydroxides as oxygen-evolution catalysts dates back to the pioneering discoveries of NiFe- and CoFe-LDHs, which revealed the synergistic effect of Fe in tuning the Ni redox states and stabilizing high-valence active species [23–27]. These early insights established the dual-metal framework that underpins modern research on NiFe-LDHs for alkaline water electrolysis. The discussion begins with the fundamental aspects of AEMWE, including the two half-reactions (i.e., HER and OER), the AEMWE cell configuration, and the key operational differences from conventional alkaline water electrolysis (AWE). Recent advances in AEM-based systems have demonstrated that non-precious catalysts can sustain industrial-level current densities under practical conditions, highlighting the potential of membrane-based electrolyzers for large-scale hydrogen production [28]. The OER reaction mechanisms in alkaline media are then addressed, followed by an outline of the performance metrics commonly employed for electrocatalyst evaluation. Particular emphasis is placed on NiFe-LDH electrocatalysts, covering diverse synthesis strategies and structural/morphological engineering approaches—namely, doping, interfacial engineering, and defect engineering—that govern their intrinsic activity and stability. The integration of NiFe-LDH catalysts into single AEMWE cells is subsequently examined, with attention to performance benchmarks and operational durability under practical conditions.

Despite rapid advances in both catalyst development and device engineering, there remains a lack of reviews that explicitly bridge the materials chemistry of NiFe-LDH catalysts with their functional performance in AEMWEs. Previous reviews have typically focused either on general alkaline OER catalysts and their fundamental reaction mechanisms [1,4,5] or on system-level design and operational aspects of AEMWE devices [6,23], but rarely on the intrinsic–extrinsic interplay between catalyst structure, reaction microenvironment, and device integration. In contrast, the present review provides a mechanistically grounded and application-oriented overview that uniquely connects three dimensions: (i) fundamental understanding of OER pathways (AEM, LOM, and emerging cooperative mechanisms) in NiFe-based systems; (ii) recent progress in doping, defect, and interfacial engineering strategies that modulate electronic structures and active-site chemistry; and (iii) practical evaluation of NiFe-LDH catalysts under single-cell AEMWE conditions. By correlating mechanistic insights with device-level performance, this work offers a timely and comprehensive perspective that guides the rational design of NiFe-LDH catalysts for scalable, non-precious-metal water electrolysis.

2. Anion Exchange Membrane Water Electrolyzer

The AEMWE has emerged as a promising route for green hydrogen production, combining the operational efficiency and compact design of proton exchange membrane electrolysis with the cost advantages and non-noble catalyst compatibility of AWE [29]. The use of polymer-based anion-conducting membranes, first explored in the late 20th century for fuel cells, has gained momentum only in the past two decades, driven by advances in ionic conductivity, chemical stability, and mechanical robustness of anion exchange membranes (AEMs) [30,31]. These improvements have enabled efficient operation under mildly alkaline electrolytes (typically ~1 M KOH or equivalent supporting salts) in a zero-gap cell configuration, where hydroxide ions (OH-) generated at the cathode migrate through the dense, non-porous AEM to the anode [32–34]. Unlike the porous diaphragms used in conventional AWE, the AEM functions simultaneously as an ionic conductor and gas separator, preventing convective crossover of hydrogen and oxygen gases while supporting continuous ion transport [35,36]. This separation yields hydrogen with purity above 99% without extensive downstream purification and allows pressurized operation with minimal recombination losses [6,37,38]. The alkaline environment further enables the deployment of non-noble metal catalysts (e.g., Ni-, Co-, and Fe-based materials) at both electrodes, along with low-cost stainless steel or Ni-based flow plates and porous transport layers—thus avoiding reliance on PGMs and titanium hardware, which are the primary cost drivers in PEMWE systems [39–41]. Additionally, the milder electrolyte reduces corrosive degradation compared to both concentrated AWE and acidic PEMWE, broadening material compatibility and lowering capital expenditure [42,43].

Operationally, AEMWE devices split water into hydrogen and oxygen via spatially separated half-reactions: cathodic water reduction to H_2 with concurrent OH^- generation, and anodic OH^- oxidation to O_2 with regeneration of water [44,45]. The solid polymer membrane enables selective ion transport, thereby conferring a fast load-following response and efficient coupling with intermittent renewable energy sources such as photovoltaic (PV) systems and wind turbines [32,46]. Recent studies confirm that AEMWE can sustain performance under fluctuating current densities, making it attractive for grid-balancing and off-grid integration [22,36,40]. Moreover, extension to alkaline seawater electrolysis has been demonstrated, where the membrane suppresses chloride crossover and chlorine evolution, enabling direct coastal and offshore hydrogen production with minimal pretreatment [32]. Ultimately, the efficiency and durability of AEMWE are dictated by the kinetics and stability of HER at the cathode and OER at the anode. In alkaline media, HER is slowed by the additional water dissociation step preceding hydrogen adsorption, while OER involves a multi-electron, multi-proton pathway with inherently sluggish kinetics [47–49]. The following sections examine these half-reactions in detail, emphasizing materials strategies, particularly NiFe-LDHs for OER, that address catalytic activity and durability in technically relevant AEMWE systems.

2.1. HER and OER in AEMWE

In AEMWE, the two essential half-reactions are HER at the cathode and OER at the anode (Equations (1)–(3)). They present distinct kinetic and material challenges due to the alkaline environment unique to the AEMWE systems. Understanding the reaction steps of overall water splitting and the specific reaction mechanisms of the HER and OER under alkaline conditions is pivotal before evaluating the catalytic performance of catalysts in an electrolyzer. The half-cell reactions under alkaline environments, together with their thermodynamic potential, are shown below:

$$\text{Cathode: } 4H_2O+4e^- \rightarrow 2H_2+4OH^- \qquad E_o = -0.828V \tag{1}$$

$$\text{Anode: } 4OH^- \rightarrow H_2O+O_2+4e^- \qquad E_o = +0.401V \tag{2}$$

$$\text{Overall: } 2H_2O \rightarrow 2H_2+O_2 \qquad E_o = 1.23V \tag{3}$$

In AEMWE, hydrogen gas is produced at the cathode, accompanied by the release of hydroxide ions, which diffuse through the anion exchange membrane toward the anode. At the anode, these OH^- ions participate in the OER, generating oxygen gas. As shown in Equation (3) [50], the overall water-splitting process requires a thermodynamic potential of approximately 1.23 V, corresponding to a Gibbs free energy change (ΔG^o) of about 237.2 kJ mol^{-1} under standard conditions (25 °C, 1 bar). In practice, the applied potential must exceed 1.23 V to overcome losses associated with mass and charge transport, electrolyte resistance, and the inherently sluggish kinetics of both HER and OER. Furthermore, the endothermic nature of the reactions contributes to additional energy losses, necessitating further input energy. This excess potential, arising from electrochemical and concentration polarization effects, is defined as the overpotential [51–53].

As for HER, it takes place at the cathode, which only involves the transfer of two electrons per H_2 produced (Equation (1)). The kinetic pathway of the HER generally follows the Volmer-Heyrovsky or Volmer-Tafel mechanism [54]. Both consist of water adsorption, followed by water dissociation (Volmer step, Equation (4)), and then either hydrogen dissociation via electrochemical desorption (Heyrovsky step, Equation (5)) or chemical desorption (Tafel step, Equation (6)) to form H_2.

$$\text{Volmer step: } H_2O+e^- \rightarrow H^*+OH^- \tag{4}$$

$$\text{Heyrovsky step: } H^*+H_2O+e^- \rightarrow H_2+OH^- \tag{5}$$

$$\text{Tafel step: } H^*+H^* \rightarrow H_2 \tag{6}$$

In Equations (4)–(6), the * indicates a surface-adsorbed species. Because breaking the H–OH bond in water requires a substantial energy, the Volmer step proceeds slowly, restricting the generation of protons for the subsequent Heyrovsky and Tafel steps [55–57]. Consequently, alkaline HER generally suffers from sluggish kinetics and demands significantly higher overpotentials compared to its acidic counterpart. Unlike the two-electron transfer involved in HER, the OER, which will be discussed in the later parts, proceeds through a multistep four-electron transfer pathway and exhibits inherently sluggish kinetics. Consequently, it is the dominant contributor to the overpotential that constrains the overall efficiency of water electrolysis.

2.2. Structure of the AEMWE Cell

Figure 1a depicts the structural configuration of an anion exchange membrane water electrolyzer in a dismantled state, highlighting its major components: end plates, bipolar plates, anode electrode with gas diffusion layer (GDL), gaskets, the anion exchange membrane, and cathode electrode with GDL [58]. The end plates provide structural integrity, maintain uniform compression, and incorporate heat management ports. The bipolar plates act as current collectors and contain integrated flow channels to ensure homogeneous electrolyte distribution and efficient gas release. The anode electrode, comprising the OER catalyst layer supported by the GDL, converts hydroxide ions to oxygen gas and water; the GDL facilitates reactant access and bubble removal. The cathode electrode, similarly supported by a GDL, hosts the HER catalyst, which generates hydrogen gas and hydroxide ions from water dissociation; here, the GDL enables efficient gas removal and minimizes transport limitations. The AEM, positioned between the electrodes, selectively conducts OH^- ions from cathode to anode while preventing gas crossover. Surrounding gaskets provide robust sealing to eliminate leakage and crosscontamination. Figure 1b illustrates the operating principles of the AEMWE [59]. At the cathode, the catholyte is reduced to hydrogen gas and OH^- ions (Equation (1)). The OH^- ions migrate across the AEM to the anode, where they are oxidized to oxygen gas and water (Equation (2)). The electrons released at the anode flow through the external circuit to the cathode, thereby completing the electrochemical cycle. This configuration allows the AEMWE to operate under alkaline conditions, enabling high-purity hydrogen production while permitting the use of inexpensive, non-precious-metal catalysts.

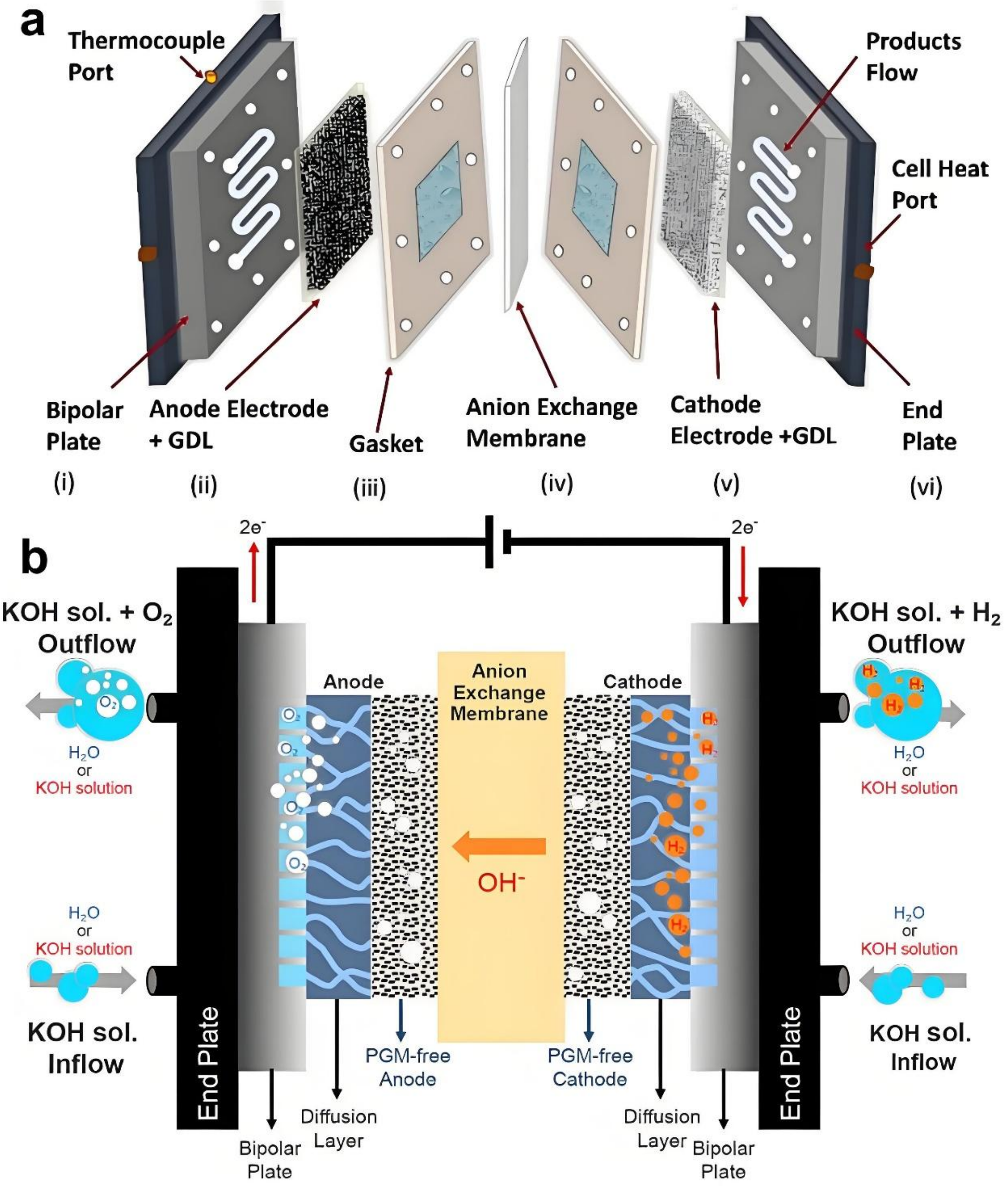

Figure 1. (**a**) Schematic diagram of a disassembled AEMWE cell. Reproduced with permission from [58], Copyright 2025, Wiley. (**b**) Schematic diagram of AEMWE working principles. Reproduced with permission from [59], Copyright 2020, Elsevier.

2.3. Key Differences between AWE and AEMWE

Traditional alkaline water electrolyzers typically employ concentrated aqueous KOH electrolytes at 25–30 wt% (5.5–6.9 M) and operate in the 65–100 °C range [60]. The anodic and cathodic compartments are separated by a porous diaphragm—initially asbestos or ceramic oxides, and more recently polymeric materials (e.g., polypropylene)—which enables ionic transport while minimizing bulk gas mixing. Nickel-based electrocatalysts are widely used owing to their favorable HER and OER kinetics in alkaline environments, combined with acceptable corrosion resistance that enables cost-effective electrodes relative to noble metals [29]. Despite these advantages, concentrated KOH imposes severe durability challenges. Its causticity accelerates corrosion of electrodes, current collectors, and balance-of-plant components, with degradation exacerbated at elevated temperatures. Moreover, exposure of circulating electrolytes to atmospheric CO_2 leads to carbonate deposition (e.g., K_2CO_3, $KHCO_3$), which consumes free hydroxide, diminishes effective alkalinity, and precipitates within or on the diaphragm [16,29,61]. Such fouling increases Ohmic resistance and impedes the mass transport, ultimately reducing the ionic conductivity and elevating cell voltage over time. These processes shorten the maintenance intervals and limit the device lifetimes.

AEMWE has emerged to address these drawbacks by combining the compact, zero-gap architecture of PEMWEs with alkaline operation compatible with non-noble catalysts. In AEMWEs, the separator is a dense anion-exchange membrane bearing covalently tethered cationic groups, most commonly quaternary ammonium moieties, along a polymer backbone [62]. This design not only eliminates the hazards associated with asbestos diaphragms but also binds mobile anions electrostatically, reducing CO_2 uptake and suppressing carbonate contamination. Compared with porous diaphragms, polymer AEM further mitigates the gas crossover, enabling safer and more compact stack designs. To limit the chemical degradation of both the cationic headgroups and polymer backbone, AEMWEs are typically operated at 40–80 °C. A distinguishing feature of AEM technology is its electrolyte flexibility. Systems may be operated with dilute KOH (0.1–1 M) or, in some configurations, with ultrapure water feeds that rely on hydroxide conduction through the hydrated membrane and ionomer phases in the catalyst layers. Lower alkalinity significantly reduces corrosion of metallic components, broadening the range of viable cell hardware and flow-field materials. The trade-off is primarily Ohmic: ionic conductivity scales with hydroxide concentration and membrane hydration. As a result, dilute electrolytes increase solution resistance and hinder interfacial ion transfer. In most experimental studies, ~1 M KOH has emerged as a practical compromise, maintaining sufficient hydroxide flux to preserve low area-specific resistance while mitigating the aggressive corrosion associated with 6 M solutions [63].

Figure 2 schematically contrasts AWE and AEMWE architectures, while Table 1 highlights the key differences in separators, operating windows, and electrolyte choices. Despite their clear system-level advantages, AEMWEs remain largely confined to laboratory and early pilot demonstrations. Two bottlenecks persist. First, the hydroxide conductivity of current AEMs and ionomers is significantly lower than that of PEM analogs, particularly at moderate temperatures and under CO_2 ingress, and their long-term chemical stability in high-pH environments remains insufficient. Second, although non-noble catalysts are economically attractive, their alkaline kinetics—especially for HER—often lag behind Pt-group benchmarks. NiFe oxides or hydroxides are the state-of-the-art catalysts for alkaline OER, whereas HER typically relies on Ni-based systems (e.g., Ni-Mo, Ni-Mo-N, Ni-Cu) that require precise microstructural tuning and robust ionomer integration to achieve low overpotentials and durable performance. The membrane–electrode assembly (MEA) integrates the AEM, catalyst-coated electrodes with anion-conducting binders, bipolar plates, and flow fields. Within the MEA, ionic transport, water management, swelling, gas removal, and catalyst–ionomer interfacial stability collectively govern performance and lifetime. Among all components, the HER and OER electrocatalysts are most critical: their intrinsic activity, transport accessibility, and resistance to dissolution or phase transformation ultimately determine AEMWE efficiency and durability. Progress in chemically robust, high-conductivity anion exchange membranes (AEMs) and ionomers, alongside advances in non-noble metal electrocatalysts and optimized electrode architectures for low-concentration electrolytes, will be central to narrowing the performance gap with PEMWEs—While preserving the cost and materials advantages inherent to alkaline electrolysis.

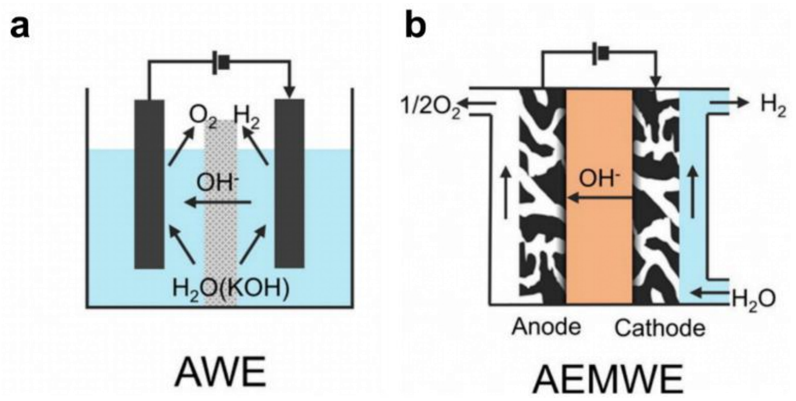

Figure 2. Schematic diagram of (**a**) conventional alkaline water electrolyzer (AWE) and (**b**) anion exchange membrane water electrolyzer (AEMWE). Reproduced with permission from [64], Copyright 2024, Elsevier.

Table 1. System differences between conventional AWE and AEMWE**.**

Characteristic	AWE [21,65,66]	AEMWE [21,62,67]
Electrolyte	5.5–6.9M KOH	0.1–1 M KOH, deionized water, ultrapure water, sea water
Operating Pressure	1–30 bar	1–30 bar
Operating Temperature (°C)	60–100 (°C)	40–80 (°C)
Cathode Catalyst	Ni-based	Pt/C, NiCo, NiMo alloys
Anode Catalyst	Ni-based	IrO_2, RuO_2, NiFe alloys
Current Density (mA/cm^2)	450–1250	100–2000 [a]
Cell Voltage (V)	1.7–2.1	1.45–2.3 [a]
Production Rate (N m^3 H_2/h)	<760	<40
Separator	Ceramic oxide, polypropylene	Anion exchange membrane
Lifetime (h)	≤100,000	≤10,000

[a] Derived from various lab-scale testing of diverse catalysts and membrane materials.

3. OER Reaction Mechanisms under Alkaline Conditions

In alkaline media, OER can follow two limiting pathways that differ in where the O–O bond forms and whether proton–electron transfer is concerted. In Figure 3a, the conventional adsorbate-evolution mechanism (AEM) is a surface sequence that converts hydroxide into a ladder of bound oxygenated intermediates on a metal site (M). A hydroxide anion first adsorbs and is oxidized to M-*OH (*represents the adsorption of the O-intermediate on M); H^+-coupled e^- removal yields M-*O_2^-; nucleophilic attack of OH^- on *O then forms M-*OOH^-, and a final deprotonation and oxidation step liberates O_2 and restores the vacant site, succinctly, OH → O → OOH → O_2 on the same active center [68,69]. Because the adsorption energies of HO*, O*, and HOO* are linearly correlated, the binding of *OH and *OOH is tied by a nearly constant difference ($\Delta G_{*OOH} - \Delta G_{*OH} \approx 3.2$ eV), which fixes a thermodynamic floor of ~370 mV for the overpotential on the RHE scale along the AEM pathway [70,71]. This correlation motivates a descriptor view: under the known scaling, the theoretical overpotential reduces to a function of ($\Delta G_{O*} - \Delta G_{OH*}$), producing a universal volcano in which the optimum is reached when the three O-intermediates are bound neither too strongly nor too weakly [72–74]. Practically, tuning composition, vacancy concentration, strain, and surface structure is used to moderate ΔG_{*O2}, ΔG_{*OH}, and ΔG_{*OOH} within this AEM landscape so that none of the four elementary steps dominates the free-energy span.

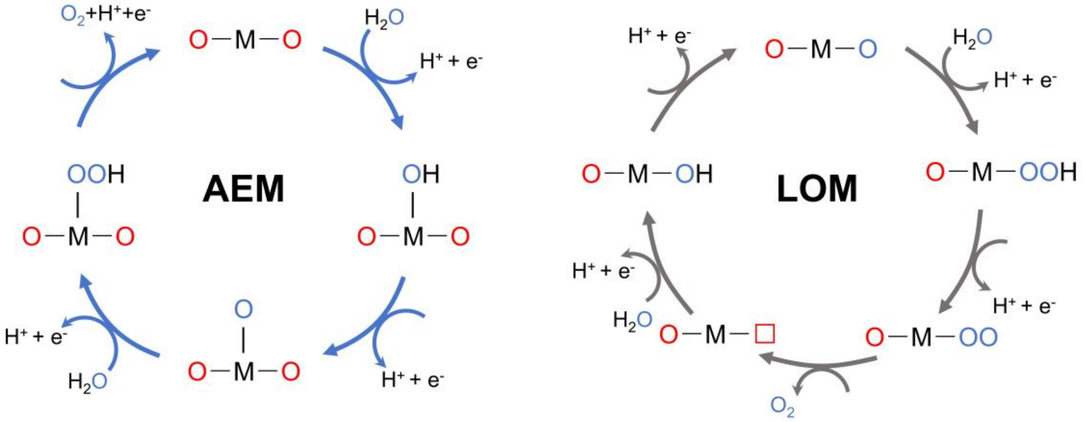

(a) **(b)**

Figure 3. Schematic illustration of the conventional AEM (**a**) and LOM (**b**) for OER, respectively. M stands for the active sites.

In Figure 3b, the alternative lattice-oxygen mechanism (LOM) shifts the locus of O–O coupling from two purely adsorbed species to a step in which the oxide lattice contributes oxygen. Once metal–oxygen covalency is sufficiently strong to make oxidation of lattice oxygen thermodynamically accessible, OER frequently proceeds through a non-concerted proton–electron transfer in which a lattice oxygen couples (with O* or an oxygenated neighbor) to form an –OO moiety, releases O_2, and leaves behind an oxygen vacancy (VO) while re-oxidizing the metal center; this can be written schematically as $O–M^{(n-1)+}–OO \rightarrow O–Mn^+\text{-}V_O + O_2 + e^-$ [75–77]. Because the O–O bond originates from lattice participation, LOM relaxes the HO*/HOO* scaling that caps the AEM pathway and can, in principle, surpass its overpotential limit [76,77]. Distinct kinetic fingerprints are often observed when LOM contributes: activity can become pH-dependent on the RHE scale and the apparent Tafel slope can drop toward 2RT/3F (40–45 mV dec^{-1} at room temperature), whereas lower characteristic slopes (RT/3F or 2RT/F) are typical of AEM-dominated kinetics [76–78]. A low slope of ≈43 mV dec^{-1} reported for $LaNiO_3$ exemplifies this lattice-assisted behavior [78]. Perovskite case studies also show that correlations between activity and pH may vary; for example, $SrCoO_{3-\delta}$ has been assigned to a lattice-oxygen pathway despite pH-independent activity, underscoring that pH trends are material-dependent and that multiple diagnostics should be weighed when assigning a mechanism.

Beyond kinetics, spectroscopy and computation indicate that, in highly covalent oxides, the thermodynamic OER potential on surface oxygen sites can approach that on metal sites, evolved O_2 can originate from lattice oxygen, and reversible formation/annihilation of oxygen vacancy (V_O) is integral to the catalytic cycle. Adsorbed O* can even diffuse into lattice sites by a nonelectrochemical pathway before O–O formation—features that are hallmarks of LOM [76]. The LOM concept extends from perovskites to (oxy)hydroxides when the electronic structure can host oxygen-non-bonding (ONB) states that stabilize peroxo/superoxo-like intermediates without destabilizing the lattice. Creating ONB states by introducing electronically filled, catalytically inactive Zn^{2+} into CoOOH increases Co–O covalency, generates oxygen holes in ONB bands along Zn–O_2–Co–O_2–Zn motifs, and biases the mechanism toward lattice involvement; the engineered $Zn_{0.2}Co_{0.8}OOH$ shows a significant specific-activity gain over undoped CoOOH [79]. Chemical-probe experiments further corroborate lattice participation on related oxyhydroxides: tetramethylammonium (TMA^+) binds strongly to in-situ-generated negative oxygen species during operation, and this binding suppresses the lattice-oxygen features and depresses activity—behavior consistent with LOM intermediates.

These two mechanistic archetypes imply complementary design philosophies. Within the AEM regime, optimization means "balancing the ladder" set by linear scaling: because $\Delta G_{*OOH} - \Delta G_{*OH}$ is effectively pinned near 3.2 eV, the actionable handle is ($\Delta G_{*O} - \Delta G_{*OH}$), which can be shifted toward the volcano summit by targeted changes in composition, defect chemistry, strain, and surface reconstruction [70–74,80–83]. By contrast, LOM-oriented design seeks to increase M–O covalency and to manage vacancy energetics so that lattice oxygen can be oxidized and reinserted without catastrophic reconstruction or cation leaching; geometric/electronic context matters as well, since octahedral coordination aligns e_g with O 2p to strengthen hybridization and facilitate O–O formation, whereas tetrahedral coordination offers weaker overlap and tends to be less active [76,77]. In practice, real catalysts often straddle these limits: high covalency and dynamic surface oxygen chemistry enable switching or blending between pathways under bias, while more ionic systems remain largely confined to the adsorbate sequence. Recognizing where a given material lies along this continuum—and using diagnostics such as descriptor-based volcano behavior (AEM) versus pH-dependent activity with low Tafel slopes and vacancy dynamics (LOM)—provides a coherent framework for rational OER optimization toward lower overpotential and sustained rates [72,74,76,77]

Beyond the well-established adsorbate evolution and lattice oxygen mechanisms, recent investigations have uncovered entirely new mechanistic paradigms for the OER on NiFe-based catalysts. These studies challenge the conventional understanding of single-site or lattice-participation pathways, instead emphasizing cooperative processes at the solid–liquid interface and dynamic restructuring of lattice oxygen ligands. In particular, the works of Kuai et al. [84] and Shi et al. [85] provide distinct perspectives that extend beyond traditional frameworks, offering fresh insights into the pivotal role of Fe species—whether dissolved or lattice-bound—in dictating OER activity. Also, recent studies have provided compelling experimental validation of lattice oxygen involvement in OER catalysis. Shao et al. [86] revealed direct isotopic evidence of boosted oxygen evolution via enhanced lattice-oxygen participation in perovskite catalysts, while Xu et al. [87] demonstrated a cation-deficiency manipulation strategy that strengthened oxygen ion diffusion and unequivocally confirmed the LOM pathway. These findings substantiate that the LOM can effectively break the conventional scaling relations of AEM by coupling bulk lattice oxygen activation with surface redox processes, offering a mechanistic foundation for designing more efficient NiFe-based catalysts. Kuai et al. reported a novel solid–molecular cooperative mechanism operative on NiFe-based hydroxides. They demonstrated that dissolved ferrate (VI) (FeO_4^{2-}) species, generated under anodic potentials, function as molecular co-catalysts in tandem with solid-state Fe centers. Operando spectroscopic evidence confirmed the presence of FeO_4^{2-}, which directly participates in the O–O bond-formation step. This dual-site relay between lattice-bound Fe and mobile FeO_4^{2-} species circumvents the conventional adsorption-energy scaling relations that restrict single-site catalysis, thereby lowering the energetic barrier for O–O coupling. This study establishes a fundamentally new pathway, distinct from both adsorbate evolution and lattice oxygen mechanisms, by elucidating the catalytic role of dissolved metal species at the solid–liquid interface.

Shi et al. uncovered another unconventional pathway in Fe-incorporated hydroxides, arising from the formation of stable lattice O–O (O_{latt}–O_{latt}) ligands. Through operando ^{18}O-labelling Raman spectroscopy, X-ray absorption spectroscopy, and mass spectrometry, they revealed that NiFe hydroxides undergo in situ transformation into a superoxo-hydroxide phase featuring long-lived O_{latt}–O_{latt} motifs. These lattice O–O ligands do not evolve directly into O_2; instead, they act as structural promoters that activate adjacent Fe centers, thereby reducing the activation barrier for the subsequent adsorbate evolution steps. Density functional theory (DFT) calculations further confirmed that O_{latt}–O_{latt} formation facilitates Fe turnover and accelerates OER kinetics. This work thus establishes a ligand-assisted catalytic pathway, fundamentally distinct from previously recognized mechanisms, underscoring the critical role of dynamic lattice oxygen coupling in modulating electrocatalytic activity. Taken together, these two emerging mechanistic paradigms suggest new strategies for catalyst design: leveraging cooperative solid–molecular interactions and stabilizing dynamic lattice O–O motifs to transcend conventional scaling relations and unlock higher OER efficiencies.

Theoretical calculations provide valuable mechanistic insights into how atomic-level modifications regulate the oxygen evolution process on NiFe-LDHs [22,88–91]. DFT-derived free-energy diagrams reveal that introducing aliovalent dopants, such as Mo or Co, effectively lowers the energy barrier of the $^*O \rightarrow {}^*OOH$ step compared with pristine NiFe-LDH, thereby accelerating the conventional adsorbate evolution mechanism [92–94]. Furthermore, the defect-engineered models indicate that oxygen vacancies modify the electronic structure by increasing metal–oxygen hybridization and generating localized states near the Fermi level, which favor lattice oxygen participation (LOM). This shift facilitates *O–O coupling through lattice oxygen, consistent with the experimentally observed activation of lattice redox species [22,95,96]. Meanwhile, interfacial configurations demonstrate that strong electronic coupling at the NiFe-LDH/oxide junction enables charge delocalization across the interface, reducing the energy difference between AEM and LOM pathways and stabilizing reaction intermediates [97–99]. Collectively, these theoretical analyses clarify that doping primarily optimizes adsorption energetics, defect formation enhances lattice oxygen activity, and interface coupling harmonizes charge redistribution, together promoting a cooperative reaction network between AEM and LOM. Such DFT-guided understanding provides a predictive framework for tuning composition, vacancy density, and heterostructure design to achieve high-efficiency, durable NiFe-LDH-based oxygen-evolution catalysts.

4. Catalyst Performance Evaluation Criteria of the OER

Well-defined and transferable metrics are essential for establishing credible benchmarks in OER electrocatalysis. Because OER is inherently sluggish and involves multiple coupled proton-electron transfer steps, careful evaluation must distinguish intrinsic catalytic activity from contributions of transport, cell resistance, or electrode degradation. Activity is commonly reported as current density at a given overpotential or vice versa, but these values must be normalized consistently, whether to geometric electrode area, electrochemically active surface area, or an estimated density of active sites. Tafel slope analysis provides mechanistic information, revealing kinetic regimes and possible rate-determining steps, while comparisons across studies require transparent reporting of experimental conditions such as pH, electrolyte composition, and reference electrode calibration. Selectivity, typically assessed through Faradaic efficiency, ensures that the measured current is genuinely associated with O_2 formation rather than side reactions. Durability metrics, including chronoamperometry, chronopotentiometry, and accelerated potential cycling, are vital to probe stability and resistance to structural transformation or leaching. Collectively, these criteria provide a rigorous framework for comparing materials and identifying genuine advances, ensuring that performance differences reflect intrinsic catalytic properties rather than experimental artifacts.

The activity of OER electrocatalysts is primarily gauged through two benchmarks, the overpotential (η) at 10 mA cm^{-2} (η_{10}) and the onset potential [100]. Accurate reporting requires explicit iR correction, since uncompensated ohmic drop can artificially elevate apparent values, particularly at higher currents [101]. Geometric-area normalization, while convenient, often conflates intrinsic catalytic activity with geometric factors such as roughness, wiring, and bubble management [102,103]. Accordingly, geometric metrics should be complemented by additional descriptors and paired with full disclosure of catalyst loading, electrolyte composition, temperature, and measurement protocols [104]. To further probe the kinetic regime, the Tafel slope is commonly derived from the relation $\eta = a + b \log|j|$ [105]. This parameter constrains mechanistic interpretation but is only reliable under steady-state conditions, as slow-sweep LSV can produce scan-rate–dependent artifacts [106]. Analysis should extend beyond RT/F (45–50 mV at 20–25 °C) yet remain within the Butler–Volmer region, as excessively high slopes ($\geq$120 mV dec^{-1}) typically signify transport or surface-state limitations [101,105,107]. In transition-metal oxyhydroxides, overlapping redox features can distort linearity; thus, slopes should be extracted from redox-free regions and validated through steady-state experiments [106].

Distinguishing between intrinsic and apparent catalytic activity requires careful normalization strategies. While mass activity (A mg^{-1}) serves as a functional techno-economic screen, it does not faithfully capture the number of catalytically competent sites. More representative measures involve normalization to electrochemically active surface area (ECSA), typically estimated via double-layer capacitance (C_{dl}) and an assumed specific capacitance (C_s). However, C_s values are not universal, spanning tens to ~130 μF cm^{-2} depending on material and pH, and self-supported electrodes may include substrate contributions. Alternative approaches, such as integration of well-resolved redox peaks that track site population or chemical probes like oxalate-based surface-area analysis, can reduce uncertainty [108,109]. Best practice is to report geometric-, ECSA-, and mass-normalized activities in parallel within the same electrolyte, thereby clarifying whether performance gains arise from true intrinsic enhancements or from surface and conductivity effects. In parallel, turnover frequency (TOF) provides a per-site metric, relating O_2 evolution to the number of active sites. However, the choice of denominator-total metal atoms, surface-accessible atoms, or electrochemically addressable sites-can alter TOF by orders of magnitude. Because site enumeration remains a significant challenge, TOF values should be treated cautiously, with preference given to current-density reporting normalized by mass or ECSA [105]. When possible, integrating distinct redox signals or applying chemical surface-area methods provides internal consistency, while gas quantification ensures that oxygen generation, rather than parasitic processes, dominates the faradaic current.

Finally, durability and selectivity remain indispensable for benchmarking electrocatalysts under realistic operating conditions. Faradaic efficiency (FE) must be quantified to confirm that faradaic charge is fully accounted for by O_2 evolution, typically through gas chromatography or collection methods, and ideally at the same operating points used for headline activity metrics [104]. Durability is commonly assessed through chronopotentiometry or chronoamperometry, reported as potential or current drift over extended periods at technologically relevant current densities (10–100 mA cm^{-2}). Accelerated aging via potential or current cycling provides deeper insights, though experimental protocols must be explicitly defined due to the lack of universal standards. Beyond conventional time-dependent drift, dissolution-aware figures of merit—such as the stability number (S-number) and the molar ratio of O_2 produced to metal dissolved—provide a quantitative measure of catalyst utilization efficiency and resilience [109]. Mechanistic attribution benefits from coupling aging tests with dissolution and impurity diagnostics, since, for nickel-based oxyhydroxides, extrinsic Fe incorporation from the electrolyte can simultaneously enhance activity and mask intrinsic stability [110,111]. Electrochemical impedance spectroscopy before and after aging provides additional resolution by separating ohmic contributions from charge-transfer or transport effects. Importantly, device-relevant testing at ≥100 mA cm^{-2} is recommended, as such regimes often reveal failure modes, heat accumulation, bubble blockage, or detachment, not captured at lower current densities. Durability assessments should therefore integrate both moderate and high-current regimes, always paired with FE measurements, to ensure that apparent stability truly reflects sustained oxygen evolution.

5. NiFe Layered-Double Hydroxide Electrocatalysts

NiFe-LDH has been recognized as a state-of-the-art OER catalyst in alkaline media, with a unique combination of intrinsic activity, electrochemical robustness, and earth-abundant constituent elements. Figure 4 [112] presents a mechanistic framework detailing the structural transformation and catalytic function of NiFe-LDH electrocatalysts during OER. Their outstanding performance is attributed to a confluence of factors, including dynamic surface restructuring, modulation of the electronic structure, and cooperative interactions between Ni and Fe centers within the LDH lattice. As illustrated in Figure 4a, anodic polarization drives the transformation of NiFe-LDH into the catalytically competent Ni(Fe)OOH phase. This process is initiated by the deprotonation of surface hydroxyl groups, particularly those bridging Ni–OH–Fe sites. Concomitantly, Ni^{2+} is oxidized to $Ni^{3+\delta}$ ($0 < \delta < 1$), giving rise to an oxyhydroxide lattice characterized by shortened metal–oxygen bonds and enhanced octahedral distortion. In situ X-ray absorption and Raman spectroscopy reveal that Fe incorporation stabilizes the transition, promoting intermediate states and facilitating the emergence of highly oxidized Ni species [113,114]. The catalytic cycle proceeds through the AEM pathway (Figure 4b), involving four sequential steps: hydroxide adsorption (*OH), oxidation to $*O_2$, nucleophilic attack forming *OOH, and O_2 release. DFT calculations demonstrate that Fe substitution shifts the Ni 3d band center downward (from −2.214 eV in NiOOH to −2.511 eV in Ni(Fe)OOH), weakening *O adsorption and lowering the overpotential for the $*O \rightarrow *OOH$ step, the rate-limiting process, from 0.50 V to 0.39 V [115–117].

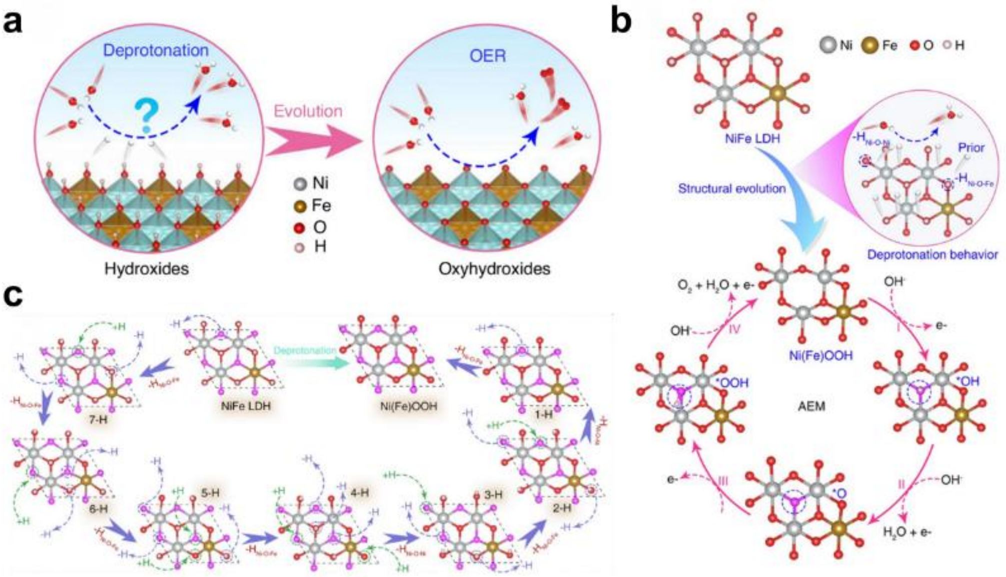

Figure 4. (**a**) Schematic of the evolution of hydroxides into oxyhydroxides during OER. (**b**) The entire deprotonation process of NiFe-LDH revealed by theoretical calculations. (**c**) Schematic of the enhanced mechanism of NiFe-LDH on alkaline OER. Reproduced with permission from [112], Copyright 2025, Springer Nature.

The thermodynamics of deprotonation, summarized in Figure 4c, further highlight the pivotal role of Fe. DFT simulations show that hydroxyl groups at the Ni–OH–Fe sites deprotonate more readily (1.13 eV) than those at Ni–OH–Ni sites (2.00 eV). Sequential removal of protons proceeds in a site-selective fashion, predominantly along Ni–Fe coordinated motifs. Overall, the energy required to fully transform NiFe-LDH into Ni(Fe)OOH is markedly lower (14.93 eV) than that for undoped $Ni(OH)_2$ (20.27 eV), underscoring the thermodynamic advantage conferred by Fe incorporation [118,119]. Collectively, these insights clarify the mechanistic origins of the remarkable OER activity of NiFe-LDHs. Iron not only accelerates lattice restructuring and proton removal but also fine-tunes the adsorption energetics of key intermediates by adjusting the electronic landscape of Ni active sites. Such synergistic regulation within the LDH framework enables the construction of catalytically competent oxyhydroxide species, thereby underpinning the superior activity of NiFe-LDH-based electrodes in alkaline water electrolysis [120].

5.1. Different Synthesis Methods for NiFe-LDH Catalysts

The OER activity of NiFe-LDHs arises from their electronic configuration and geometric architecture, yet fine control over these parameters remains challenging due to the complex coupling of composition, morphology, and reactivity. Accordingly, recent efforts have focused on constructing NiFe-LDHs with precisely defined features—including elemental composition, morphology, crystal phase, and surface defect states—through synthetic strategies such as sol–gel processing, solid-state synthesis, hydrothermal crystallization, and co-precipitation. These approaches enable rational tuning of structural and electronic attributes, establishing clear structure–activity correlations that drive enhanced catalytic performance (Figure 5). Solid-state routes employ Ni/Fe precursors in the solid phase, where diffusion is activated by mechanical grinding and mild heating. These methods are solvent-free, inherently scalable, and have recently been shown to yield LDH nanosheets with competitive OER activity when milling parameters and post-aging conditions are carefully optimized [121,122]. Sol–gel synthesis relies on the hydrolysis or chelation of Ni/Fe salts to achieve molecular-level mixing. Subsequent drying and mild thermal treatment, followed by rehydration, produce LDH platelets with high compositional homogeneity. The Fe^{3+} content can be finely tuned in this route and correlates with enhanced OER activity, although precise control over pH and ligand ratios is required [123,124].

Hydrothermal synthesis remains the most widely used approach for fabricating binder-free electrodes. In this method, Ni^{2+}/Fe^{3+} salts crystallize with a slow OH^- source, typically urea, to form ultrathin LDH nanosheets that can be directly deposited on Ni foam, thereby minimizing interfacial resistance and enabling high areal current densities. Reaction time, temperature, and the inclusion of additives such as F^- or sulfides govern nanosheet density and thickness [125]. Co-precipitation provides the most straightforward, room-temperature route and applies to both powders and inks. Increasing the pH induces the co-precipitation of Ni/Fe hydroxide layers while simultaneously incorporating interlayer anions such as CO_3^{2-}, NO_3^-, or functional species. Recent studies confirm that this approach is compatible with scalable, atmospheric-pressure fabrication suitable for device integration [88,126]. Overall, solid-state and sol–gel methods emphasize compositional homogeneity and compatibility with continuous processing, hydrothermal synthesis affords self-supported electrodes with tunable nanostructures, and co-precipitation offers a balance between simplicity and interlayer-chemistry control for high-performance OER powders. Hydrothermal growth on Ni foam currently represents the state of the art for practical electrode architectures, while room-temperature co-precipitation is emerging as a promising pathway toward scale-up without sacrificing catalytic activity [125–127]. Some other representative synthetic approaches for NiFe-LDH preparation include room-temperature precipitation and epoxide-mediated hydrolysis routes, alkoxide-assisted methods, and moderate-temperature hydrolysis strategies that enable fine control of crystallinity and metal dispersion. Chelating agents such as triethanolamine have also been used to regulate nucleation and layer growth. These diverse methods have been systematically summarized in recent studies [24,88–91].

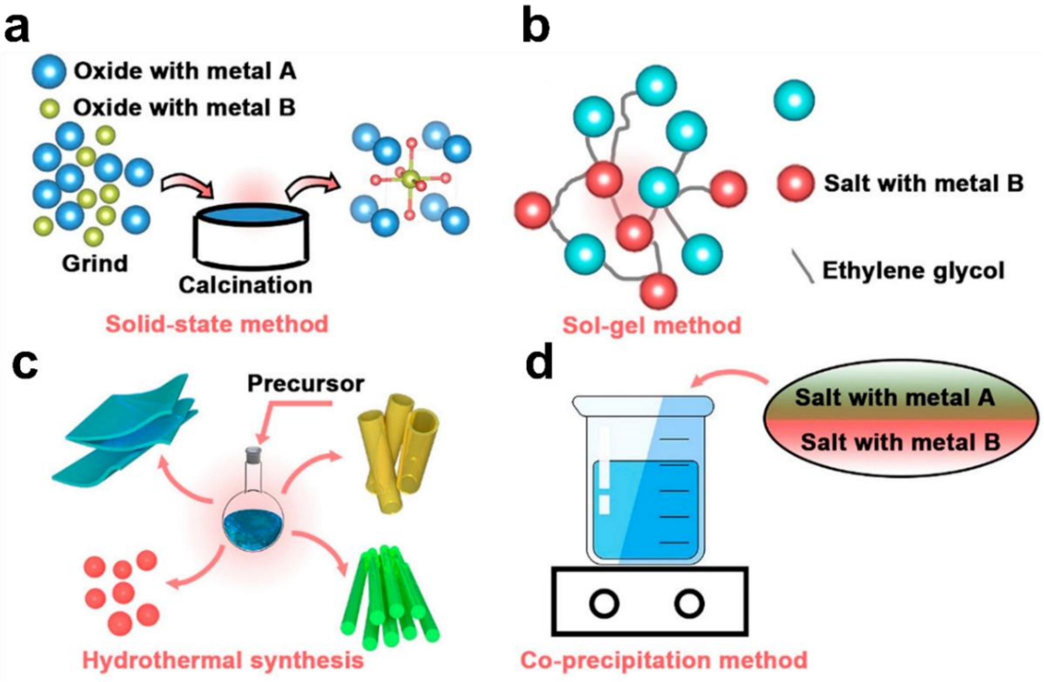

Figure 5. Schematic of the main synthesis processes for NiFe-LDH, including the (**a**) solid-state method; (**b**) sol–gel method; (**c**) hydrothermal synthesis; and (**d**) coprecipitation method. Reproduced with permission from [110], Copyright 2022, American Chemical Society.

5.2. Structure and Morphology Control

5.2.1. Defect Engineering

Defect engineering in NiFe-based electrocatalysts demonstrates a versatile toolkit for tuning catalytic behavior through vacancies, lattice distortions, and structural disorder. Zhang et al. [92] applied plasma treatment deliberately to induce structural disorder and generate abundant cation and oxygen vacancies within NiFe-LDH nanosheets. As shown in Figure 6a, HRTEM imaging reveals blurred and discontinuous lattice fringes, which are characteristic of vacancy formation and partial amorphization. These structural defects significantly increase the number of undercoordinated Ni and Fe atoms, thereby providing additional sites that can function as highly active centers for the OER. Beyond structural evidence, impedance spectroscopy confirmed that these defective surfaces enhance the ECSA and accelerate charge transfer between the catalyst and the electrolyte. On the computational side, Figure 6b illustrates DFT free-energy diagrams showing that vacancy-rich NiFe reduces the barrier for the *O–*OOH step, which is usually the rate-determining step in pristine NiFe-LDHs. By tuning the adsorption energies, the vacancies allow *OOH to bind more strongly while moderating the overly strong binding of *O, ultimately creating a more favorable reaction pathway. This mechanism explains the small Tafel slope observed and the overpotential of 290 mV at 100 mA cm^{-2}, coupled with excellent stability under long-term operation. Importantly, the structural defects are not simply random damage but serve as intentional modifications that reshape the local coordination and electronic environment. In doing so, they lower kinetic barriers, improve conductivity, and provide catalytic flexibility, transforming NiFe-LDH into a more efficient and robust OER catalyst.

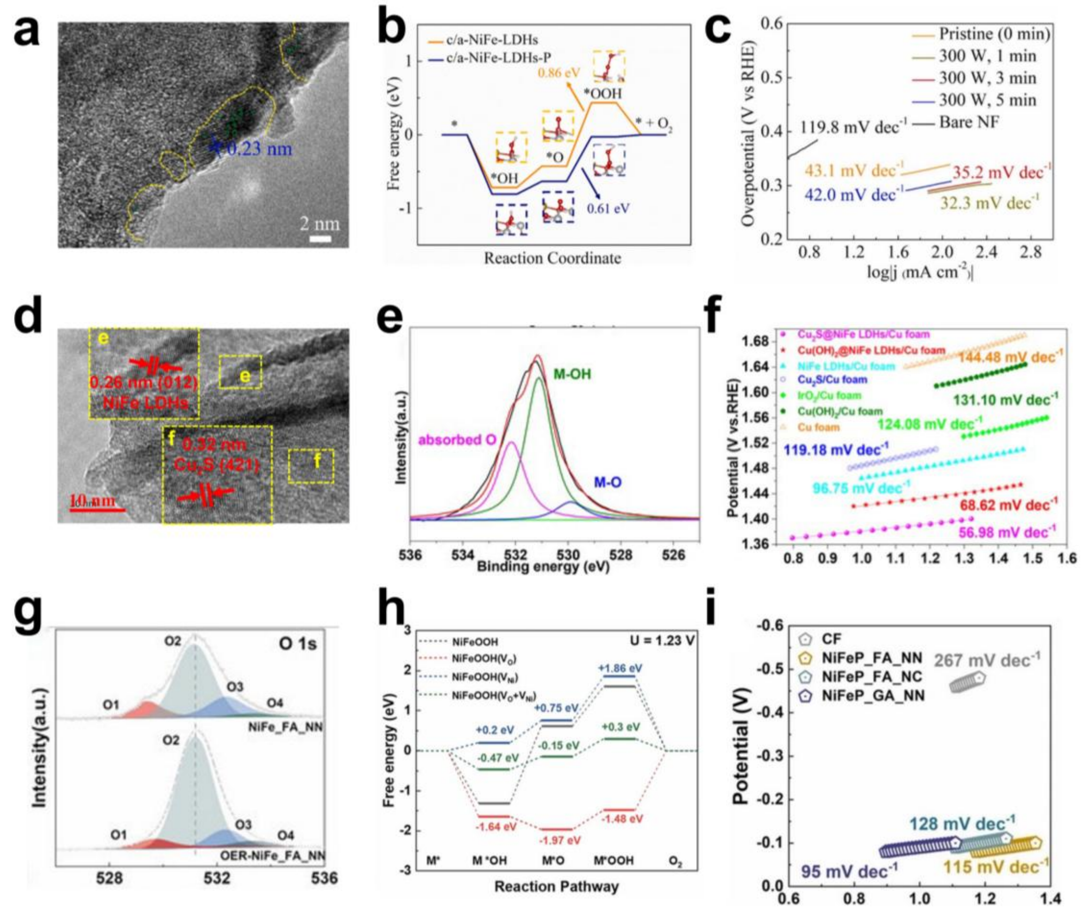

Figure 6. (**a**) HRTEM image of c/a-NiFe-LDHs-P@300:1. (**b**) DFT free energy diagram of intermediates in OER on c/a-NiFe-LDHs and c/a-NiFe-LDHs-P surfaces. (**c**) Tafel slopes of c/a-NiFe-LDHs-P@300:Y (Y = 0, 1, 3, and 5 min, respectively). Figure 6a–c reproduced with permission from [92], Copyright 2025, Elsevier. (**d**) TEM images of the Cu_2S@NiFe LDHs/Cu foam electrode. (**e**) high-resolution XPS of O 1s. (**f**) Tafel slopes of different electrodes. Figure 6d−f reproduced with permission from [93], Copyright 2023, Elsevier. (**g**) O 1s XPS spectra of NiFe_FA_NN before and after OER. (**h**) Gibbs free energy diagram of NiFeOOH with different crystal structures along the OER reaction pathway. (**i**) Tafel slopes of as-deposited NiFeP catalysts with different set-ups and nickel salts performed in 1.0 M KOH. Figure 6g-I reproduced with permission from [94], Copyright 2023, Elsevier.

The Cu_2S@NiFe LDH composite, reported by Guo et al. [93], was designed through a Kirkendall process that transformed copper foam into hollow Cu_2S nanorods, which were subsequently coated with ultrathin NiFe-LDH nanosheets. Figure 6d confirms the hollow interiors and disordered lattice edges of the Cu_2S cores, which serve as reservoirs for structural defects. These features not only expose a high density of catalytically active sites but also enhance charge-carrier mobility throughout the system. The conductive Cu_2S core acts as an efficient electron-transport pathway, while the NiFe-LDH shell provides abundant surface sites for oxygen evolution. This core–shell synergy ensures that the electrons generated at the active NiFe sites are quickly transported away, minimizing resistance and enhancing kinetics. On the theoretical side, Figure 6e presents high-resolution XPS of O 1s orbitals, which demonstrates substantial interfacial electron redistribution between Cu_2S and NiFe-LDH. This redistribution optimizes OH^- adsorption and lowers the overall energy barrier of the OER process. Electrochemical testing validates these advantages, showing an overpotential of 228 mV at 10 mA cm^{-2} with a Tafel slope of 56.98 mV dec^{-1} in Figure 6f, indicative of rapid kinetics. The hollow structure additionally facilitates mass transport of reactants and products, reducing bubble accumulation and ensuring more efficient operation. Taken together, the Cu_2S@NiFe LDH system exemplifies how defect-rich heterostructures can combine structural conductivity, abundant vacancies, and interfacial synergy to yield excellent catalytic activity and durability.

In another study published by Wei et al. [94], a self-evolving multi-vacancy strategy was developed, where electrodeposition in a nitrate-based eutectic solvent was followed by electrochemical activation to produce NiFe catalysts. These catalysts were capable of dynamically generating vacancies during operation, ensuring a continuous supply of active sites under OER conditions. As shown in Figure 6g, O 1s XPS spectra reveal a significant increase in vacancy-related peaks after activation, confirming the creation of oxygen-deficient environments. Unlike static vacancies formed during synthesis, these defects continue to evolve during electrocatalysis, ensuring persistence and regeneration of catalytic activity. The vacancies enhance electronic conductivity, allowing for rapid charge transfer between the electrode and electrolyte. On the computational side, Figure 6h shows DFT free-energy diagrams, which demonstrate that NiFe surfaces containing both Ni and O vacancies exhibit compressed energy profiles for the formation of *OOH intermediates, thereby lowering the RDS barrier. This mechanism accounts for the outstanding performance metrics: an overpotential of only 230 mV at 10 mA cm^{-2}, 115 mV dec^{-1}, and stable operation for more than 100 h at industrial current densities, with negligible degradation. The key innovation lies in the dynamic character of the vacancies, which regenerate and adapt to reaction conditions, ensuring that the catalyst does not lose activity over time. This self-evolving behavior represents a new paradigm in defect engineering, highlighting how controlled disorder can be harnessed to build catalysts that are both efficient and highly durable.

Across the studies, characterization techniques such as HRTEM and XPS confirm the presence of defects: plasma treatment produces oxygen and cation vacancies in NiFe-LDH; Kirkendall synthesis creates hollow Cu_2S nanostructures with lattice disorder; and electrochemical activation generates self-evolving multi-vacancies. These different pathways share a unifying outcome—creation of unsaturated coordination sites and enhanced charge-transfer channels. On the electronic level, DFT consistently shows that defects reduce the barrier of the *O–*OOH step, often the RDS in pristine NiFe catalysts. Vacancies rebalance adsorption energies, weakening overly strong *O binding while stabilizing *OOH intermediates, thereby improving the overall reaction energetics. In addition, interfacial disorder enhances conductivity, allowing electrons to flow more efficiently between active sites and substrates. This synergy of increased active-site density and improved electronic transport creates a dual pathway for performance enhancement. The electrochemical results align strongly with these structural insights. Defect-rich catalysts routinely deliver overpotentials below 250–300 mV at 10 mA cm^{-2}, with Tafel slopes often below 40 mV dec^{-1}, demonstrating accelerated kinetics. More importantly, dynamic or self-evolving vacancies ensure that activity is maintained under prolonged operation, even at industrial current densities. Thus, defect engineering does not merely "damage" the catalyst structure but rationally introduces controlled disorder to enhance performance. By creating unsaturated sites and enabling flexible lattice responses, defects make NiFe-based catalysts highly adaptive under reaction conditions, resulting in superior activity, efficiency, and stability.

5.2.2. Doping Engineering

Mo incorporation into NiFe (oxy)hydroxide is convincingly demonstrated in Figure 7a, where the XPS Mo 3d spectrum clearly identifies Mo states, accompanied by shifts in Ni and Fe binding energies [95]. These changes confirm that Mo atoms are substitutionally incorporated into the NiFe lattice rather than forming segregated surface phases. This distinction is vital because substitutional doping directly alters the electronic structure of the host, while surface segregation has only limited effects. The catalytic consequences are illustrated in Figure 7b, which presents DFT free-energy diagrams comparing pristine and Mo-doped NiFe. In the pristine case, the rate-determining step is oxygen vacancy formation, but upon Mo incorporation, the RDS shifts to *OOH deprotonation, which requires a substantially lower energy barrier. This change reflects a more favorable pathway that accelerates the adsorbate evolution mechanism while introducing partial lattice oxygen involvement. Structurally, Mo atoms enhance electronic delocalization across the lattice, while electronically they fine-tune adsorption energies of oxygen intermediates, ensuring neither *O nor *OOH are over-stabilized. Electrochemical studies confirm these predictions, with Mo-doped NiFe delivering a nearly 60-fold increase in mass activity compared with undoped NiFe. The catalyst achieves low overpotentials and long-term operational stability, showing that Mo doping not only improves intrinsic site activity but also stabilizes high-valent Ni and Fe centers during operation. Together, these results highlight how carefully chosen dopants can induce both structural and electronic adjustments at the atomic level, creating catalysts with enhanced kinetics, durability, and efficiency for oxygen evolution.

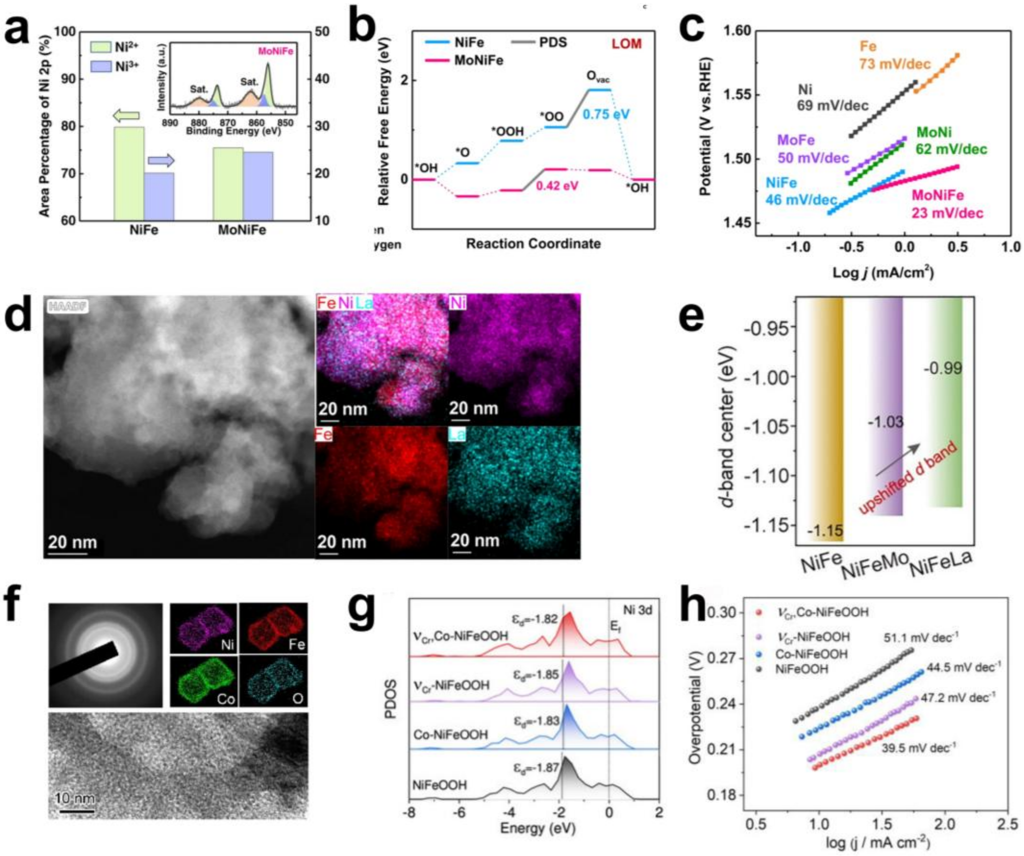

Figure 7. (**a**) Oxidation state of nickel in NiFe and MoNiFe (oxy)hydroxide determined by Ni 2p XPS. (**b**) DFT free energy diagrams of the LOM pathway on NiFe and MoNiFe (oxy)hydroxide. (**c**) Tafel slopes of MoNiFe (oxy)hydroxide. Figure 7a–c reproduced with permission from [95], Copyright 2022, Springer Nature. (**d**) HAADF-STEM image with elemental mappings of NiFeLa. (**e**) d-band center of adsorbed atoms in the NiFe, NiFeMo, and NiFeLa. Figure 7d,e reproduced with permission from [96], Copyright 2024, Springer Nature. (**f**) SAED pattern, elemental mapping, and HRTEM image of V_{Cr},Co-NiFeOOH. (**g**) PDOS d-band center of Ni 3d orbitals from V_{Cr},Co-NiFeOOH, V_{Cr}-NiFeOOH, Co-NiFeOOH, and NiFeOOH. (**h**) Tafel slopes of the four catalysts. Figure 7f–h reproduced with permission from [22], Copyright 2025, American Chemical Society.

The incorporation of La into NiFe-LDH is confirmed in Figure 7d, where HAADF-STEM images combined with EDS mapping show the homogeneous distribution of La with Ni and Fe [96]. This uniform distribution rules out clustering or phase segregation, providing strong evidence that La is genuinely incorporated into the NiFe lattice. The large ionic radius of La and its available 5d orbitals induce local lattice distortions and create new orbital overlaps with Ni and Fe centers. These structural modifications alter the electronic environment in ways that enhance catalytic activity. Theoretical validation comes from Figure 7e, which shows an upward shift in the d-band center, from −1.15 eV in pristine NiFe to −0.99 eV in La-doped NiFe. This shift means stronger *OOH adsorption but without excessive stabilization of *O intermediates, thereby optimizing the reaction energetics. Significantly, La doping also stabilizes high-valent Ni and Fe species during OER cycling, preventing deactivation and dissolution. Electrochemical data further confirm the benefits: La-doped NiFe achieves an ultralow overpotential of ~185 mV at 10 mA cm^{-2}, a Tafel slope of 35 mV dec^{-2}, and operational stability extending beyond 600 h at high current density. These results underscore how La, though catalytically inactive itself, modifies the local coordination structure to create an electronically optimized and structurally stabilized catalyst. By coupling lattice distortion with orbital interactions, La doping demonstrates how non-redox-active dopants can drastically enhance both the activity and durability of NiFe-based OER systems.

Co incorporation into NiFeOOH nanocages, discovered by Niu et al. [22], is directly evidenced in Figure 7f, where TEM combined with EDS mapping reveals homogeneous Co distribution throughout the framework. This provides unambiguous proof of actual substitutional doping, as opposed to surface segregation or clustering. The unique nanocage morphology, with its high surface area and porous structure, facilitates mass transport of both reactants and products, enabling efficient utilization of the doped active sites. The electronic impact of Co doping is shown in Figure 7g, where DFT projected density of states (PDOS) analyses reveal a subtle upshift of the Ni 3d band center from −1.87 to −1.82 eV. This adjustment strengthens *OH adsorption at Ni centers, while simultaneously weakening Fe–O interactions. The combined effect is a balancing of dual-site catalysis between Ni and Fe, optimizing their respective roles in the OER process. By lowering the energy barrier of the RDS, this modification ensures more efficient electron transfer and intermediate turnover. Electrochemically, the Co-doped NiFeOOH achieves an overpotential of just 198 mV at 10 mA cm^{-2} and maintains stability for over 500 h, even under high current operation. These results highlight the advantage of redox-active dopants such as Co, which can actively participate in electronic redistribution while maintaining a balanced catalytic environment. By rebalancing dual-site activity and leveraging structural porosity, Co-doped NiFeOOH exemplifies how targeted doping strategies can translate into superior OER performance, combining high activity, durability, and efficient mass transport.

Doping strategies clearly demonstrate how substitutional incorporation of heteroatoms systematically modifies the intrinsic properties of NiFe-based catalysts. Structural evidence from XPS, STEM-EDS, and TEM mapping verifies successful doping of Mo, La, and Co into the NiFe lattice, ruling out segregated phases. Such atomic-level incorporation ensures that changes to catalytic behavior originate from electronic modulation within the active framework rather than surface impurities. Theoretical insights consistently show dopant-induced shifts in the d-band center and rebalanced adsorption energies for OER intermediates. Mo activates lattice oxygen and shifts the RDS to *OOH deprotonation, drastically boosting mass activity. La induces lattice distortion and 3d–5d orbital coupling, optimizing *OOH binding while stabilizing high-valent species, which explains both low overpotentials and remarkable durability. Co subtly shifts the Ni 3d band center, rebalancing dual-site activity between Ni and Fe, leading to efficient and stable catalysis. Electrochemically, these doped materials exhibit some of the most competitive performance metrics reported for NiFe catalysts: overpotentials well below 200 mV at 10 mA cm^{-2}, Tafel slopes around 30–40 mV dec^{-1}, and operational lifetimes exceeding hundreds of hours. The catalytic activity of NiFe-LDHs is also strongly influenced by the Ni:Fe molar ratio. Studies generally report optimal activity when the Ni content exceeds Fe, typically in the range of Ni:Fe = 3:1–4:1, which favors the formation of highly active Ni^{3+}/Ni^{2+} redox couples and improves electrical conductivity. In contrast, Fe-rich or near-stoichiometric LDHs (Ni:Fe = 1:1–2:1) often exhibit enhanced long-term stability and more homogeneous metal dispersion. A balanced Ni:Fe ratio is therefore critical to achieving both activity and durability under alkaline OER and AEMWE conditions. The unifying theme is that doping offers atom-level control over electronic structure, enabling precise tuning of intermediate adsorption and improved charge transfer. In practice, this translates into catalysts that approach or surpass noble-metal standards while retaining cost advantages. Doping engineering thus stands as a powerful, versatile, and rational strategy for advancing NiFe-based OER electrocatalysts.

5.2.3. Interfacial Engineering

Wu et al. [97] reported that d-(Fe,Ni)OOH nanosheets inherently contain a high density of phase boundaries and stacking faults, which function as interfacial defects that enhance catalytic performance. As shown in Figure 8a, HRTEM images reveal these irregular structures, which increase structural heterogeneity and establish electronic highways across domains. These interfacial regions promote rapid electron transfer and redistribute charges across neighboring active sites, effectively modulating the local coordination environment. The catalytic role of these interfaces is further supported by Figure 8b, where DFT charge-density difference maps highlight electron polarization concentrated at the defect boundaries. This redistribution relaxes the scaling relation between *O and *OOH adsorption, effectively lowering the energy barrier for the RDS. The optimized electronic structure allows more active centers to participate in OER simultaneously, improving catalytic turnover. Electrochemical measurements show that d-(Fe,Ni)OOH achieves a low overpotential of 236 mV at 10 mA cm^{-2} with a Tafel slope between 21.7 mV cm^{-1} and 44.0 mV cm^{-1}, and demonstrates robust stability during prolonged testing. The key innovation here lies in transforming internal defects, traditionally considered structural weaknesses, into functional interfacial sites that drive electron transport and stabilize intermediates. This demonstrates how tailoring the microstructural interface can unlock performance gains by fine-tuning adsorption energetics and enhancing conductivity, thereby accelerating OER kinetics and ensuring long-term durability.

Researched by Wu et al. [98], a deliberate interfacial heterojunction was engineered between crystalline Ni_4Mo particles and amorphous NiFe-LDH nanosheets. As shown in Figure 8d, HRTEM images confirm intimate contact between the two components, ensuring the formation of nanoscale interfaces. These interfaces establish a cooperative division of labor, where the conductive Ni_4Mo serves as an electron-rich domain while NiFe-LDH provides abundant catalytically active sites. The mechanistic advantage is captured in Figure 8e, where DFT calculations reveal that OH^- adsorption is energetically favored on Ni_4Mo, followed by transfer of oxygen intermediates to NiFe-LDH. This so-called “oxygen pump” effect accelerates lattice oxygen regeneration while simultaneously suppressing Ni and Fe dissolution, which is a common cause of catalyst degradation. The cooperative interfacial mechanism results in both improved activity and durability: the heterojunction catalyst achieves an overpotential of ~193 mV at 10 mA cm^{-2} and a Tafel slope of 42 mV cm^{-1} (Figure 8f), and maintains stable operation for more than 150 h in AEMWE. The integration of Ni_4Mo with NiFe-LDH thus provides a compelling demonstration of how rational heterostructure design can overcome both kinetic limitations and structural instability, leveraging interfacial synergy to achieve superior OER performance.

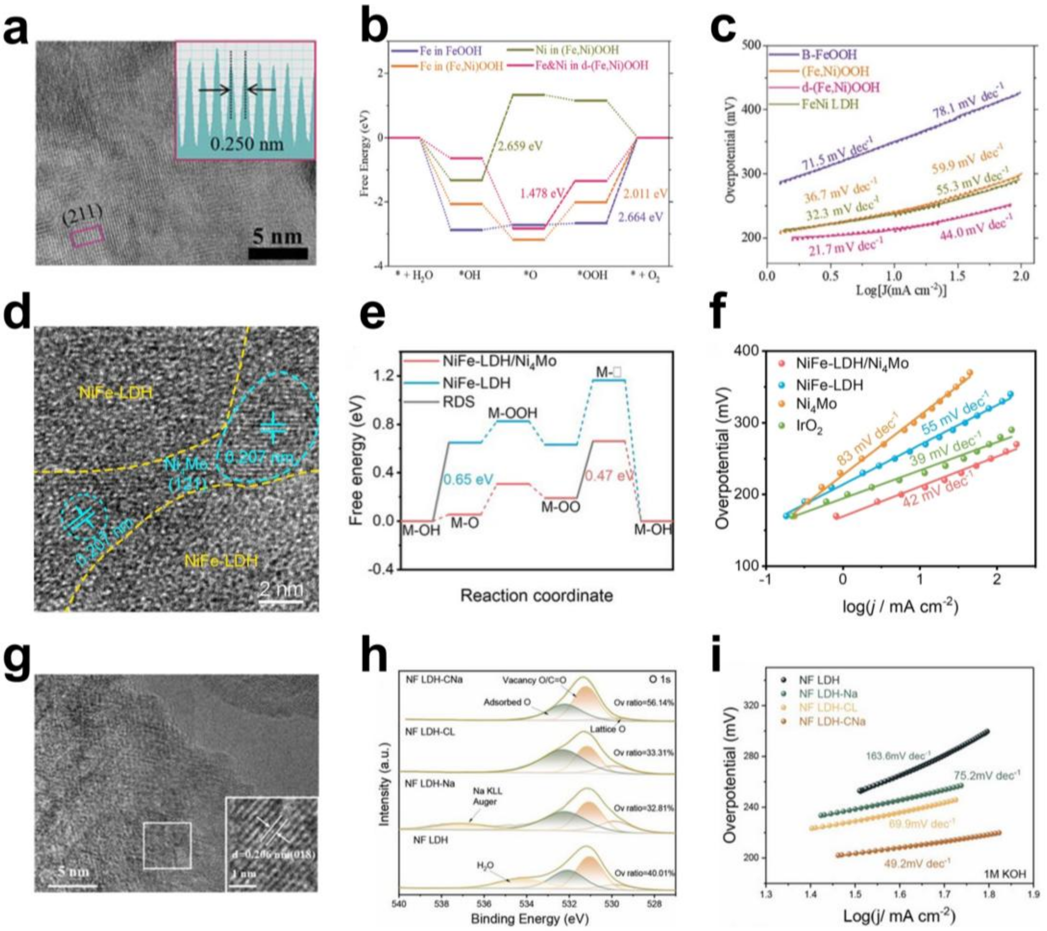

Figure 8. (**a**) HRTEM image of d-(Fe,Ni)OOH. Inset: interplanar spacing of the lattice fringe marked by the rectangle in (**a**). (**b**) DFT Free energy diagram for the OER process of d-(Fe,Ni)OOH. (**c**) Tafel slopes of d-(Fe,Ni)OOH. Figures 8a–c were reproduced with permission from [97], Copyright 2023, Wiley. (**d**) HRTEM image of NiFe-LDH/Ni_4Mo. (**e**) DFT free energy diagram for the OER through AEM steps. (**f**) Tafel slopes of NiFe-LDH/Ni_4Mo. Figures 8d–f were reproduced with permission from [98], Copyright 2025, Wiley. (**g**) HRTEM images of NF LDH-cNa. (**h**) XPS of O 1s of the NF LDH-cNa. (**i**) Tafel slopes of NF LDH-cNa. Figures 8g–i were reproduced with permission from [99], Copyright 2026, Elsevier.

Zhang et al. [99] explored interfacial engineering through local coordination modification, using Na^+ ions and carboxylate ligands to alter the electronic environment of NiFe-LDH nanosheets. As shown in Figure 8g, elemental mapping demonstrates the uniform incorporation of Na^+ and carboxylates, confirming successful surface modification across the entire catalyst. Unlike bulk doping, this strategy focuses on tuning the coordination environment at the interface between the catalyst and the electrolyte. The electronic impact is demonstrated in Figure 8h, where XPS of O 1s orbitals shows three distinct oxygen environments: adsorbed oxygen species (O_w) at 532.2 eV, oxygen vacancies or low-coordination oxygen sites (O_v) at 531.2 eV, and lattice metal–oxygen bonds (M-O) at 529.9 eV. Notably, the NF LDH-cNa sample exhibits the largest fraction of Ov (56.14%), indicating a higher concentration of defect sites and exposed edge terminations generated through the dual modification strategy. The successful incorporation of Na^+ is further supported by an Auger signal at 537.02 eV detected in the NF LDH-Na sample. In contrast, the NF LDH spectrum shows a peak at 534.2 eV, which can be attributed to surface-adsorbed water molecules or free hydroxyl groups. The modified NiFe-LDH exhibits an ultralow overpotential of ~194 mV at 10 mA cm^{-2}, a Tafel slope of 49.2 mV cm^{-1}, and maintains excellent stability under long-term seawater electrolysis. The combination of ligand coordination and cation incorporation fine-tunes the electronic structure without altering the bulk lattice, showing that subtle interfacial modifications can have a dramatic impact on both activity and stability. This case extends the concept of interfacial engineering beyond structural junctions or phase boundaries to include chemical coordination environments, thereby broadening the design toolkit for advanced OER catalysts.

Interfacial engineering demonstrates the breadth of strategies that exploit structural boundaries and coordination environments to optimize OER performance. Structural probes such as HRTEM and EDS mapping confirm the presence of phase boundaries, heterojunctions, and ligand-modified coordination sites, while DFT simulations reveal how these interfaces redistribute charge, stabilize intermediates, and relax scaling relations. Mechanistically, the approaches differ but converge in outcome. In d-(Fe,Ni)OOH, interfacial defects act as electronic highways, polarizing active sites and lowering RDS barriers. In Ni_4Mo/NiFe-LDH heterojunctions, the interface facilitates cooperative catalysis, where Ni_4Mo captures and pumps oxygen intermediates to NiFe-LDH, boosting both activity and stability through the "oxygen pump" effect. In Na^+/carboxylate-modified NiFe-LDH, ligand coordination introduces local polarization, stabilizing high-valent states and providing resilience against chloride corrosion. Each pathway underscores the importance of treating interfaces as active contributors rather than structural byproducts. Electrochemically, these interfacial systems deliver outstanding metrics: overpotentials below 200–240 mV at 10 mA cm^{-2}, small Tafel slopes, and extended stability even under seawater or AEMWE operation. Importantly, interfacial design tackles both intrinsic kinetics and extrinsic stability challenges, making it uniquely versatile compared with doping or defect-only strategies. By constructing functional contact points at the atomic, nanoscale, or molecular level, interfacial engineering enables synergistic effects that cannot be achieved by lattice modification alone. Thus, interfacial engineering emerges as a complementary and essential pillar of NiFe catalyst design, offering robust solutions for high-efficiency oxygen evolution. Beyond half-cell investigations, recent studies have demonstrated that NiFe-LDH catalysts can be effectively integrated into complete AEMWE systems, validating their practical applicability for large-scale hydrogen production.

While the above strategies—including elemental doping, defect creation, and interfacial modulation—have markedly improved the intrinsic OER activity of NiFe-LDH catalysts, their ultimate validation lies in integration within complete AEMWE systems. Recent studies have advanced beyond conventional three-electrode testing to directly evaluate NiFe-LDH-based catalysts in single-cell or short-stack configurations, providing critical insight into catalyst–ionomer–membrane compatibility and the influence of electrode architecture on mass transport and durability. Among these, doping has proven especially effective in tuning the electronic structure and promoting active-phase reconstruction under realistic conditions. Representative examples further demonstrate the promise of NiFe-based catalysts in practical AEMWEs. He et al. developed a bifunctional MoS_2/NiFe-LDH‖MoNiFe cell sustaining 100 mA cm^{-2} at 1.728 V for over 20 h [95]. Wang et al. constructed a $NiFeLa_{0.5}$‖Pt/C electrolyzer achieving 1 A cm^{-2} at 1.58 V with 600-h stability at 80 °C [96], and Niu et al. reported a V_{Cr},Co–NiFeOOH‖Pt–NiCoP system delivering 500 mA cm^{-2} at 1.69 V for 500 h at 25 °C [22]. Collectively, these findings reveal that compositional tuning and interfacial design can effectively translate laboratory-scale activity into durable, high-current-density performance in full-cell configurations. Heteroatom incorporation further facilitates lattice oxygen activation, accelerates charge transfer, and stabilizes high-valence Ni species crucial for sustained OER. Such advances bridge the gap between materials development and device-level implementation, highlighting the potential of NiFe-LDH-derived catalysts for efficient, scalable AEM water electrolysis.

6. Electrocatalysts in a Single AEMWE Cell

A comprehensive comparison of diverse NiFe-LDH electrocatalysts is presented as listed in Table 2, where their operational metrics, namely, working current density (mA cm^{-2}), applied cell voltage (V), and long-term durability are systematically evaluated. The results clearly demonstrate that variations in synthetic strategy, coupled with deliberate morphology regulation (e.g., nanosheets, nanoflakes, or hierarchical architectures) [128,129], exert a decisive influence on the intrinsic catalytic activity and overall device performance. Subtle modifications in structural features, including layer thickness, surface exposure of active sites, and defect density, in turn dictate electron/ion transport kinetics and stability under prolonged operation. In addition, the overall efficiency of AEMWE is determined by ionic conductivity and interfacial contact between components, as highlighted in recent device-level studies [130,131]. Consequently, the collective evidence highlights the critical role of both synthesis methodology and morphological engineering in tailoring the electrocatalytic behavior of NiFe-LDHs for oxygen evolution and related applications.

Table 2. Comparison of the catalytic performances of anode materials [22,40,93,132–148].

Anode	Current Density (mA · cm^{-2})	Voltage (V)	Durability (h)	Ref.
V_{Cr}, Co-NiFeOOH	500	1.69	500	22
NiFe-LDH-PTA	1000	1.93	170	40
Cu_2S@NiFe-LDH/Cu foam	500	1.56	300	93
Ni_2P-Fe/NF	1000	1.73	24	132
Ni-doped FeOOH	729	1.7	15	133
S-$CoCuO_x$/NF	1000	1.87	110	134
NiFeV LDH/HF	2100	1.8	100	135
$Cu_{0.81}Co_{2.19}O_4$/NF	100	1.68	100	136
$FCM_{0.47}$/Ni-felt	1560	1.8	500	137
$NiFe(OH)_x/Fe_2O_3$NAs/CC	600	1.75	200	138
CuCo-oxide/NF	1390	1.8	64	139
Ruc/NiFe-LDH	1000	2.08	120	140
Co:NiFe-LDH@PVA	400	2.04	100	141
FePi-NiS/NF	500	2.1	30	142
NiFe-TCPP	500	2.68	88	143
$Ni_xFe_yMo_z$ LDH	1000	2.1	20	144
S-NiFe-LDH	500	2.5	200	145
Fe_2O_3/NiFe-LDHs	100	1.6	50	146
NiFeCo-OOH	500	1.65	300	147
NiFeCr-LDH/NF	500	1.79	40	148

7. Summary and Perspectives

Anion-exchange-membrane water electrolysis integrates a zero-gap configuration with alkaline operation, enabling the use of earth-abundant anodes and shifting performance control toward the catalyst–ionomer–membrane microenvironment. Comparative studies consistently identify NiFe-LDHs and their oxyhydroxide derivatives as leading oxygen-evolution catalysts in alkaline media. Their advantage arises from dual-site interactions in which Fe modulates the Ni redox landscape, stabilizes high-valence states, and adjusts oxygenated intermediate binding relative to single-site analogs. Recent advances increasingly focus on engineering the microenvironment at the active interface rather than bulk composition. Three complementary strategies have emerged. Elemental doping adjusts d-band positions and site polarity by introducing aliovalent species. Defect engineering generates vacancy fields that relax over-binding, redistribute charge, and mitigate lattice strain. Interface design shortens ion and electron pathways while pre-polarizing sites at junctions. These levers converge in dual-site optimization paradigms, where dopants enhance adsorption on Ni while vacancies weaken adsorption on Fe, jointly aligning binding energies and lowering the barrier of the rate-determining step. Spectroscopic and electrochemical evidence corroborates this cooperative tuning, linking higher Ni valence, redistributed charge density, and reduced charge-transfer resistance to durable single-cell operation. At the device level, voltage decomposition reveals contributions from electrode kinetics, high-frequency resistance, catalyst-layer ohmic losses, and ion-exchange resistance. Within the anode, further partitioning identifies penalties from bubble accumulation, local alkalinity shifts, and intrinsic kinetics. This framework clarifies why materials that accelerate charge transfer, regulate wettability, and preserve open gas pathways can simultaneously suppress multiple loss channels. Demonstrations of stable operation at ampere-class current densities for thousands of hours are promising, yet reproducibility remains limited by diverse MEA designs, testing conditions, and reporting practices. Standardized single-cell protocols and in-operando diagnostics are urgently needed to establish reproducible performance baselines [149,150].

The principal bottlenecks for NiFe-LDHs in AEM electrolyzers are now well defined. Phase reconstruction of the active layer must be rapid yet controlled, as elevated temperatures and pH gradients accelerate metal dissolution and particle coarsening [151]. The modest intrinsic conductivity of hydroxide phases necessitates conductive, corrosion-resistant backbones; otherwise, catalyst layers thicken electrically and underutilize buried sites. The catalyst–ionomer interface remains a weak link, where chemical mismatch and poor wetting generate dead zones and elevate ionic resistance. Oxygen management is another constraint, with bubble accumulation demanding hierarchical porosity and controlled wettability. System-level issues—including carbonate uptake, collector corrosion, and membrane dehydration—further confound performance unless tracked with in-operando partitioning. A lack of harmonized degradation criteria continues to obscure the distinction between reversible and irreversible losses. Accelerating progress requires coupling atomic-level tuning to mechanistic regimes of oxygen evolution. The classical adsorbate-evolution pathway favors moderated metal–oxygen binding and balanced intermediate stabilization, whereas mechanisms involving lattice oxygen necessitate vacancy tolerance and efficient defect healing. Both regimes can be steered through dopant incorporation, vacancy control, and near-surface electric fields. Future microenvironment engineering should therefore localize dopants and defects at regions influencing the outer Helmholtz plane, enabling efficient charge redistribution and interfacial transport without compromising structural stability. Dual-site paradigms remain especially promising, reinforcing adsorption on Ni while weakening it on Fe—a cooperative mechanism validated by both theory and experiment. Catalyst layers must be regarded as integrated ionic–electronic–gas transport media rather than passive coatings. Rational design should align ionomer chemistry with catalyst surface charge, set ionomer fraction to balance utilization with pore accessibility, and introduce hierarchical porosity that couples nanometer-scale water/ion transport with micron-scale gas release [152]. These multifunctional architectures require evaluation via impedance and voltage partitioning, not polarization curves alone. Robust backbones such as self-supported porous metals, conductive nitrides or sulfides, and ordered hollow frameworks will be essential to maintain conductivity and mechanical stability under oxidative load.

Finally, testing and diagnostics must evolve alongside materials. Recommended practices include break-in procedures, slow-sweep polarization curves, durability tests exceeding 1000 h, and dynamic stress profiles that separate reversible from irreversible degradation. In-operando methods such as impedance and voltage partitioning are indispensable for assigning performance drift to specific degradation modes. As systems move toward higher operating temperatures, membranes and ionomers must sustain conductivities near $0.1\ \mathrm{S \cdot cm^{-1}}$ while retaining chemical stability above 60 °C, a persistent materials challenge directly coupled to anode and cathode durability. Balanced electrode development is also critical: while NiFe anodes dominate among non-noble catalysts, alkaline hydrogen evolution at the cathode remains a bottleneck, with standardized cathode protocols urgently required. In conclusion, NiFe layered hydroxides have progressed from compositional candidates to catalysts engineered with a mechanistic rationale and growing device relevance. Future advances will hinge on integrating dual-site regulation, vacancy-tuned defect chemistry, and coherent interface design into catalyst layers that are thin, conductive, wettable, and gas-permeable, all validated under harmonized protocols with in-operando diagnostics. Aligning materials chemistry, transport architecture, and evaluation methodology presents the most direct pathway to durable, scalable AEM water electrolyzers based on nickel–iron hydroxide backbones.

Funding

This work was supported by the National Natural Science Foundation of China (22509085, 22402081, and 92472117), China National Postdoctoral Program for Innovative Talents (BX20250441), China Postdoctoral Science Foundation (2025M774272), and the Open Foundation of Shanghai Jiao Tong University Shaoxing Research Institute of Renewable Energy and Molecular Engineering (Grant No. JDSX2023019). C.L. acknowledges the National Natural Science Foundation of China (52302231 and 22479034) and the Key Research & Development Plan of Heilongjiang Province (2024ZXJ03C06). This work is also supported by the Jiangsu Funding Program for Excellent Postdoctoral Talent.

Data Availability Statement

The data generated during this study are available in the main text.

Conflicts of Interest

The authors declare no conflict of interest.

Use of AI and AI-Assisted Technologies

No AI tools were utilized for this paper.

References

1. Du, N.; Roy, C.; Peach, R.; et al. Anion Exchange Membrane Water Electrolyzers. *Chem. Rev.* **2022**, *122*, 11830–11895.
2. Zhang, R.; Hanaoka, T. Cross-Cutting Scenarios and Strategies for Designing Decarbonization Pathways in the Transport Sector toward Carbon Neutrality. *Nat. Commun.* **2022**, *13*, 3629.
3. Zou, C.; Xiong, B.; Xue, H.; et al. The Role of New Energy in Carbon Neutral. *Pet. Explor. Dev.* **2021**, *48*, 480–491.
4. Kanan, M.W.; Surendranath, Y.; Nocera, D.G. Cobalt–Phosphate Oxygen-Evolving Compound. *Chem. Soc. Rev.* **2008**, *38*, 109–114.

5. Suntivich, J.; May, K.J.; Gasteiger, H.A.; et al. Perovskite Oxide Optimized for Oxygen Evolution Catalysis from Molecular Orbital Principles. *Science* **2011**, *334*, 1383–1385.
6. David, M.; Ocampo-Martínez, C.; Sánchez-Peña, R. Advances in Alkaline Water Electrolyzers: A Review. *J. Energy Storage* **2019**, *23*, 392–403.
7. Sebbahi, S.; Assila, A.; Alaoui Belghiti, A.; et al. A Comprehensive Review of Recent Advances in Alkaline Water Electrolysis for Hydrogen Production. *Int. J. Hydrogen Energy* **2024**, *82*, 583–599.
8. Xu, Y.; Cai, S.; Chi, B.; et al. Technological Limitations and Recent Developments in a Solid Oxide Electrolyzer Cell: A Review. *Int. J. Hydrogen Energy* **2024**, *50*, 548–591.
9. Lin, C.; Li, J.-L.; Li, X.; et al. *In-Situ* Reconstructed Ru Atom Array on α-MnO_2 with Enhanced Performance for Acidic Water Oxidation. *Nat. Catal.* **2021**, *4*, 1012–1023.
10. Wu, Z.Y.; Chen, F.Y.; Li, B.; et al. Non-Iridium-Based Electrocatalyst for Durable Acidic Oxygen Evolution Reaction in Proton Exchange Membrane Water Electrolysis. *Nat. Mater.* **2023**, *22*, 100–108.
11. King, L.A.; Hubert, M.A.; Capuano, C.; et al. A Non-Precious Metal Hydrogen Catalyst in a Commercial Polymer Electrolyte Membrane Electrolyser. *Nat. Nanotechnol.* **2019**, *14*, 1071–1074.
12. Li, G.; Yu, Y.; Wang, C.; et al. Core-Shell Structured V-Doped CoP_x@FeOOH for Efficient Seawater Electrolysis. *ChemCatChem* **2025**, *17*, e00850.
13. Henkensmeier, D.; Cho, W.C.; Jannasch, P.; et al. Separators and Membranes for Advanced Alkaline Water Electrolysis. *Chem. Rev.* **2024**, *124*, 6393–6443.
14. Niether, C.; Faure, S.; Bordet, A.; et al. Improved Water Electrolysis Using Magnetic Heating of FeC–Ni Core–Shell Nanoparticles. *Nat. Energy* **2018**, *3*, 476–483.
15. Wang, J.; Gao, Y.; Kong, H.; et al. Non-Precious-Metal Catalysts for Alkaline Water Electrolysis: Operando Characterizations, Theoretical Calculations, and Recent Advances. *Chem. Soc. Rev.* **2020**, *49*, 9154–9196.
16. Tang, Z.; Wu, B.; Yan, K.; et al. Long-Term Stability for Anion Exchange Membrane Water Electrolysis: Recent Development and Future Perspectives. *Future Batter.* **2025**, *5*, 100024.
17. Li, W.; Li, F.; Yang, H.; et al. A Bio-Inspired Coordination Polymer as Outstanding Water Oxidation Catalyst via Second Coordination Sphere Engineering. *Nat. Commun.* **2019**, *10*, 5074.
18. Park, S.; Liu, L.; Demirkır, Ç.; et al. Solutal Marangoni Effect Determines Bubble Dynamics during Electrocatalytic Hydrogen Evolution. *Nat. Chem.* **2023**, *15*, 1532–1540.
19. Zheng, W.; He, L.; Tang, T.; et al. Poly(Dibenzothiophene-Terphenyl Piperidinium) for High-Performance Anion Exchange Membrane Water Electrolysis. *Angew. Chem.* **2024**, *63*, e202405738.
20. Kumar, R.; Singh, R.; Dutta, S. Review and Outlook of Hydrogen Production through Catalytic Processes. *Energy Fuels* **2024**, *38*, 2601–2629.
21. Vincent, I.; Bessarabov, D. Low Cost Hydrogen Production by Anion Exchange Membrane Electrolysis: A Review. *Renew. Sustain. Energy Rev.* **2018**, *81*, 1690–1704.
22. Niu, H.J.; Ran, N.; Zhou, W.; et al. Synergistic Atomic Environment Optimization of Nickel-Iron Dual Sites by Co Doping and Cr Vacancy for Electrocatalytic Oxygen Evolution. *J. Am. Chem. Soc.* **2025**, *147*, 2607–2615.
23. Gong, M.; Li, Y.; Wang, H.; et al. An Advanced Ni-Fe Layered Double Hydroxide Electrocatalyst for Water Oxidation. *J. Am. Chem. Soc*. **2013**, *135*, 8452–8455.
24. Abellán, G.; Carrasco, J.A.; Coronado, E.; et al. Alkoxide-Intercalated CoFe-Layered Double Hydroxides as Precursors of Colloidal Nanosheet Suspensions: Structural, Magnetic and Electrochemical Properties. *J. Mater. Chem. C* **2014**, *2*, 3723–3731.
25. Carrasco, J.A.; Sanchis-Gual, R.; Silva, A.S.-D.; et al. Influence of the Interlayer Space on the Water Oxidation Performance in a Family of Surfactant-Intercalated NiFe-Layered Double Hydroxides. *Chem. Mater*. **2019**, *31*, 6798–6807.
26. Zhao, Y.; Zhang, X.; Jia, X.; et al. Sub-3 nm Ultrafine Monolayer Layered Double Hydroxide Nanosheets for Electrochemical Water Oxidation. *Adv. Energy Mater*. **2018**, *8*, 1703585.
27. Song, F.; Hu, X. Exfoliation of Layered Double Hydroxides for Enhanced Oxygen Evolution Catalysis. *Nat. Commun.* **2014**, *5*, 4477.
28. Tang, J.; Xu, X.; Tang, T.; et al. Perovskite-Based Electrocatalysts for Cost-Effective Ultrahigh-Current-Density Water Splitting in Anion Exchange Membrane Electrolyzer Cell. *Small Methods* **2022**, *6*, 2201099.
29. Dekel, D.R. Review of Cell Performance in Anion Exchange Membrane Fuel Cells. *J. Power Sources* **2018**, *375*, 158–169.
30. Couture, G.; Alaaeddine, A.; Boschet, F.; et al. Polymeric Materials as Anion-Exchange Membranes for Alkaline Fuel Cells. *Prog. Polym. Sci.* **2011**, *36*, 1521–1557.
31. Villagra, A.; Millet, P. An Analysis of PEM Water Electrolysis Cells Operating at Elevated Current Densities. *Int. J. Hydrogen Energy* **2019**, *44*, 9708–9717.
32. Park, Y.S.; Jeong, J.-Y.; Jang Myeong, M.J.; et al. Ternary Layered Double Hydroxide Oxygen Evolution Reaction Electrocatalyst for Anion Exchange Membrane Alkaline Seawater Electrolysis. *J. Energy Chem.* **2022**, *75*, 127–134.

33. Vincent, I.; Kruger, A.; Bessarabov, D. Development of Efficient Membrane Electrode Assembly for Low Cost Hydrogen Production by Anion Exchange Membrane Electrolysis. *Int. J. Hydrogen Energy* **2017**, *42*, 10752–10761.
34. Li, W.; Ding, Y.; Zhao, Y.; et al. Zwitterion-Modified NiFe OER Catalyst Achieving Ultrastable Anion Exchange Membrane Water Electrolysis via Dynamic Alkaline Microenvironment Engineering. *Angew. Chem.* **2025**, *64*, e202505924.
35. Koper, M.T.M. Thermodynamic Theory of Multi-Electron Transfer Reactions: Implications for Electrocatalysis. *J. Electroanal. Chem.* **2011**, *660*, 254–260.
36. Lin, G.; Dong, A.; Li, Z.; et al. An Interlayer Anchored NiMo/MoO_2 Electrocatalyst for Hydrogen Evolution Reaction in Anion Exchange Membrane Water Electrolysis at High Current Density. *Adv. Mater.* **2025**, *37*, 2507525.
37. Vincent, I.; Lee, E.-C.; Kim, H.-M. Highly Cost-Effective Platinum-Free Anion Exchange Membrane Electrolysis for Large Scale Energy Storage and Hydrogen Production. *RSC Adv.* **2020**, *10*, 37429–37438.
38. Grigoriev, S.A.; Fateev, V.N.; Bessarabov, D.G.; et al. Current Status, Research Trends, and Challenges in Water Electrolysis Science and Technology. *Int. J. Hydrogen Energy* **2020**, *45*, 26036–26058.
39. Du, J.; Li, Z.; Wang, L.; et al. Anion Exchange Membrane Seawater Electrolysis at 1.0 A cm^{-2} With an Anode Catalyst Stable for 9000 H. *Adv. Sci.* **2025**, *12*, e2416661.
40. Zhang, J.; Zhang, X.; Ma, Z.; et al. POM-Intercalated NiFe-LDH as Enhanced OER Catalyst for Highly Efficient and Durable Water Electrolysis at Ampere-Scale Current Densities. *ACS Catal.* **2025**, *15*, 6486–6496.
41. Cui, X.; Ding, Y.; Tang, T.; et al. Hierarchical $NiFeMoO_4$ Precatalyst Reconstructed NiFeOOH Anodes for Efficient and Durable Anion-Exchange Membrane Water Electrolysis. *ACS Appl. Mater. Interfaces* **2025**, *17*, 29659–29668.
42. Mirabella, F.; Müllner, M.; Touzalin, T.; et al. Ni-Modified Fe_3O_4(001) Surface as a Simple Model System for Understanding the Oxygen Evolution Reaction. *Electrochim. Acta* **2021**, *389*, 138638.
43. Oener, S.Z.; Foster, M.J.; Boettcher, S.W. Accelerating Water Dissociation in Bipolar Membranes and for Electrocatalysis. *Science* **2020**, *369*, 1099–1103.
44. Zeng, K.; Zhang, D. Recent Progress in Alkaline Water Electrolysis for Hydrogen Production and Applications. *Prog. Energy Combust. Sci.* **2010**, *36*, 307–326.
45. Ma, X.; Zhao, J.; Shou, D.; et al. A Highly-Flexible and Breathable Photo-Thermo-Electric Membrane for Energy Harvesting. *Adv. Energy Mater.* **2024**, *14*, 2470067.
46. Jiang, T.; Jiang, X.; Jiang, C.; et al. Novel Fe-Modulating Raney-Ni Electrodes toward High-Efficient and Durable AEM Water Electrolyzer. *Adv. Energy Mater.* **2025**, *15*, 2501634.
47. Trasatti, S. Electrocatalysis in the Anodic Evolution of Oxygen and Chlorine. *Electrochim. Acta* **1984**, *29*, 1503–1512.
48. Seh, Z.W.; Kibsgaard, J.; Dickens, C.F.; et al. Combining Theory and Experiment in Electrocatalysis: Insights into Materials Design. *Science* **2017**, *355*, 4998.
49. McCrory, C.C.L.; Jung, S.; Peters, J.C.; et al. Benchmarking Heterogeneous Electrocatalysts for the Oxygen Evolution Reaction. *J. Am. Chem. Soc.* **2013**, *135*, 16977–16987.
50. Lamy, C.; Millet, P. A Critical Review on the Definitions Used to Calculate the Energy Efficiency Coefficients of Water Electrolysis Cells Working under Near Ambient Temperature Conditions. *J. Power Sources* **2020**, *447*, 227350.
51. Wang, T.; Xie, H.; Chen, M.; et al. Precious Metal-Free Approach to Hydrogen Electrocatalysis for Energy Conversion: From Mechanism Understanding to Catalyst Design. *Nano. Energy* **2017**, *42*, 69–89.
52. Wang, M.; Yan, C.; Liu, T.; et al. Enhancing Built-In Electric Field via Balancing Interfacial Atom Orbit Hybridization at Boride@Sulfide Heterostructure for Hydrogen Evolution Reaction. *Angew. Chem., Int. Ed.* **2025**, *64*, e202425657.
53. Li, J.; Zheng, G. One-Dimensional Earth-Abundant Nanomaterials for Water-Splitting Electrocatalysts. *Adv. Sci.* **2017**, *4*, 1600380.
54. Lei, C.; Wang, Y.; Hou, Y.; et al. Efficient Alkaline Hydrogen Evolution on Atomically Dispersed Ni–N_x Species Anchored Porous Carbon with Embedded Ni Nanoparticles by Accelerating Water Dissociation Kinetics. *Energy Environ. Sci.* **2019**, *12*, 149–156.
55. Zhu, J.; Hu, L.; Zhao, P.; et al. Recent Advances in Electrocatalytic Hydrogen Evolution Using Nanoparticles. *Chem. Rev.* **2020**, *120*, 851–918.
56. Shi, Y.; Zhang, B. Recent Advances in Transition Metal Phosphide Nanomaterials: Synthesis and Applications in Hydrogen Evolution Reaction. *Chem. Soc. Rev.* **2016**, *45*, 1529–1541.
57. Li, Y.; Pei, W.; He, J.; et al. Hybrids of PtRu Nanoclusters and Black Phosphorus Nanosheets for Highly Efficient Alkaline Hydrogen Evolution Reaction. *ACS Catal.* **2019**, *9*, 10870–10875.
58. Nsanzimana, J.M.V.; Cai, L.; Djire, A.; et al. Tailoring Chemical Microenvironment of Iron-Triad Electrocatalysts for Hydrogen Production by Water Electrolysis. *Adv. Energy Mater.* **2025**, *15*, 2501686.
59. Park, H.J.; Lee, S.Y.; Lee, T.K.; et al. N3-butyl Imidazolium-Based Anion Exchange Membranes Blended with Poly (vinyl alcohol) for Alkaline Water Electrolysis. *J. Membr. Sci.* **2020**, *611*, 118355.
60. Ursua, A.; Gandia, L.M.; Sanchis, P. Hydrogen Production from Water Electrolysis: Current Status and Future Trends. *Proc. IEEE* **2012**, *100*, 410–426.

61. Naughton, M.S.; Brushett, F.R.; Kenis, P.J.A. Carbonate Resilience of Flowing Electrolyte-Based Alkaline Fuel Cells. *J. Power Sources* **2011**, *196*, 1762–1768.
62. Miller, H.A.; Bouzek, K.; Hnat, J.; et al. Green Hydrogen from Anion Exchange Membrane Water Electrolysis: A Review of Recent Developments in Critical Materials and Operating Conditions. *Sustain. Energy Fuels* **2020**, *4*, 2114–2133.
63. Pushkareva, I.V.; Pushkarev, A.S.; Grigoriev, S.A.; et al. Comparative Study of Anion Exchange Membranes for Low-Cost Water Electrolysis. *Int. J. Hydrogen Energy* **2020**, *45*, 26070–26079.
64. Ham, K.; Bae, S.; Lee, J. Classification and Technical Target of Water Electrolysis for Hydrogen Production. *J. Energy Chem.* **2024**, *95*, 554–576.
65. Felgenhauer, M.; Hamacher, T. State-of-the-Art of Commercial Electrolyzers and on-Site Hydrogen Generation for Logistic Vehicles in South Carolina. *Int. J. Hydrogen Energy* **2015**, *40*, 2084–2090.
66. Navarro, R.M.; Guil, R.; Fierro, J.L.G. Introduction to Hydrogen Production. In *Compendium of Hydrogen Energy*; Subramani, V., Basile, A., Veziroğlu, T.N., Eds.; Woodhead Publishing: Oxford, UK, 2015; pp. 21–61.
67. Motealleh, B.; Liu, Z.; Masel, R.I.; et al. Next-Generation Anion Exchange Membrane Water Electrolyzers Operating for Commercially Relevant Lifetimes. *Int. J. Hydrogen Energy* **2021**, *46*, 3379–3386.
68. Dau, H.; Limberg, C.; Reier, T.; et al. The Mechanism of Water Oxidation: From Electrolysis via Homogeneous to Biological Catalysis. *ChemCatChem* **2010**, *2*, 724–761.
69. Li, J. Oxygen Evolution Reaction in Energy Conversion and Storage: Design Strategies Under and Beyond the Energy Scaling Relationship. *Nano Micro Lett.* **2022**, *14*, 112.
70. Cui, X.; Ren, P.; Deng, D.; et al. Single Layer Graphene Encapsulating Non-Precious Metals as High-Performance Electrocatalysts for Water Oxidation. *Energy Environ. Sci.* **2016**, *9*, 123–129.
71. Craig, M.J.; Coulter, G.; Dolan, E.; et al. Universal Scaling Relations for the Rational Design of Molecular Water Oxidation Catalysts with Near-Zero Overpotential. *Nat. Commun.* **2019**, *10*, 4993.
72. Zhang, L.; Zhu, H.; Hao, J.; et al. Integrating the Cationic Engineering and Hollow Structure Engineering into Perovskites Oxides for Efficient and Stable Electrocatalytic Oxygen Evolution. *Electrochim. Acta* **2019**, *327*, 135033.
73. Liu, H.J.; Chiang, C.Y.; Wu, Y.S.; et al. Breaking the Relation between Activity and Stability of the Oxygen-Evolution Reaction by Highly Doping Ru in Wide-Band-Gap $SrTiO_3$ as Electrocatalyst. *ACS Catal.* **2022**, *12*, 6132–6142.
74. Qi, J.; Zhang, Y.; Liu, H.; et al. Strain Modified Oxygen Evolution Reaction Performance in Epitaxial, Freestanding, and Van Der Waals Manganite Thin Films. *Nano Lett.* **2022**, *22*, 7066–7072.
75. Song, J.; Wei, C.; Huang, Z.F.; et al. A Review on Fundamentals for Designing Oxygen Evolution Electrocatalysts. *Chem. Soc. Rev.* **2020**, *49*, 2196–2214.
76. Grimaud, A.; Diaz-Morales, O.; Han, B.; et al. Activating Lattice Oxygen Redox Reactions in Metal Oxides to Catalyse Oxygen Evolution. *Nat. Chem.* **2017**, *9*, 457–465.
77. Hwang, J.; Rao, R.R.; Giordano, L.; et al. Perovskites in Catalysis and Electrocatalysis. *Science* **2017**, *358*, 751–756.
78. Hardin, W.G.; Mefford, J.T.; Slanac, D.A.; et al. Tuning the Electrocatalytic Activity of Perovskites through Active Site Variation and Support Interactions. *Chem. Mater.* **2014**, *26*, 3368–3376.
79. Huang, Z.-F.; Song, J.; Du, Y.; et al. Chemical and Structural Origin of Lattice Oxygen Oxidation in Co–Zn Oxyhydroxide Oxygen Evolution Electrocatalysts. *Nat. Energy* **2019**, *4*, 329–338.
80. Siahrostami, S.; Villegas, S.J.; Bagherzadeh Mostaghimi, A.H.; et al. A Review on Challenges and Successes in Atomic-Scale Design of Catalysts for Electrochemical Synthesis of Hydrogen Peroxide. *ACS Catal.* **2020**, *10*, 7495–7511.
81. Ling, T.; Yan, D.Y.; Jiao, Y.; et al. Engineering Surface Atomic Structure of Single-Crystal Cobalt (II) Oxide Nanorods for Superior Electrocatalysis. *Nat. Commun.* **2016**, *7*, 12876.
82. Zhuang, L.; Ge, L.; Yang, Y.; et al. Ultrathin Iron-Cobalt Oxide Nanosheets with Abundant Oxygen Vacancies for the Oxygen Evolution Reaction. *Adv. Mater.* **2017**, *29*, 1606793.
83. Petrie, J.R.; Cooper, V.R.; Freeland, J.W.; et al. Enhanced Bifunctional Oxygen Catalysis in Strained $LaNiO_3$ Perovskites. *J. Am. Chem. Soc.* **2016**, *138*, 2488–2491.
84. Kuai, C.; Liu, L.; Hu, A.; et al. Dissolved Fe Species Enable a Cooperative Solid–Molecular Mechanism for the Oxygen Evolution Reaction on NiFe-Based Catalysts. *Nat. Catal.* **2025**, *8*, 523–535.
85. Shi, G.; Li, J.; Lu, T.; et al. Lattice O–O Ligands in Fe-Incorporated Hydroxides Enhance Water Oxidation Electrocatalysis. *Nat. Chem.* **2025**, *17*, 1607–1614.
86. Pan, Y.; Xu, X.; Zhong, Y.; et al. Direct Evidence of Boosted Oxygen Evolution over Perovskite by Enhanced Lattice Oxygen Participation. *Nat. Commun.* **2020**, *11*, 2002.
87. Xu, X.; Pan, Y.; Zhong, Y.; et al. New Undisputed Evidence and Strategy for Enhanced Lattice-Oxygen Participation of Perovskite Electrocatalyst through Cation Deficiency Manipulation. *Adv. Sci*. **2022**, *9*, 2200530.
88. Seijas-Da Silva, A.; Hartert, A.; Oestreicher, V.; et al. Scalable Synthesis of NiFe-Layered Double Hydroxide for Efficient Anion Exchange Membrane Electrolysis. *Nat. Commun.* **2025**, *16*, 6138.

89. Abellán, G.; Coronado, E.; Martí-Gastaldo, C.; et al. Hexagonal Nanosheets from the Exfoliation of Ni^{2+}-Fe^{3+} LDHs: A Route towards Layered Multifunctional Materials. *J. Mater. Chem.* **2010**, *20*, 7451–7455.
90. Carrasco, J.A.; Romero, J.; Varela, M.; et al. Alkoxide-Intercalated NiFe-Layered Double Hydroxides Magnetic Nanosheets as Efficient Water Oxidation Electrocatalysts. *Inorg. Chem. Front.* **2016**, *3*, 478–487.
91. Jaramillo-Hernández, C.; Seijas-Da Silva, A.; Abellán, G. Crystallographic Phase-Dependent Electrochemical Properties of Layered Hydroxides for Energy Applications. *Eur. J. Inorg. Chem.* **2025**, *28*, e202400754.
92. Zhang, D.; Ou, S.; Chang, X. Synergistic Effect of Defect Engineering and Crystalline/Amorphous Interfaces in NiFe Layered Double Hydroxides for Efficient Oxygen Evolution. *J. Alloy Compd.* **2025**, *1036*, 182010.
93. Guo, D.; Yu, H.; Chi, J.; et al. Cu_2S@NiFe Layered Double Hydroxides Nanosheets Hollow Nanorod Arrays Self-Supported Oxygen Evolution Reaction Electrode for Efficient Anion Exchange Membrane Water Electrolyzer. *Int. J. Hydrogen Energy* **2023**, *48*, 17743–17757.
94. Wei, Z.; Guo, M.; Zhang, Q. Scalable Electrodeposition of NiFe-Based Electrocatalysts with Self-Evolving Multi-Vacancies for High-Performance Industrial Water Electrolysis. *Appl. Catal. B Environ.* **2023**, *322*, 122101.
95. He, Z.; Zhang, J.; Gong, Z.; et al. Activating Lattice Oxygen in NiFe-Based (oxy)Hydroxide for Water Electrolysis. *Nat. Commun.* **2022**, *13*, 2191.
96. Wang, X.; Pi, W.; Hu, S.; et al. Boosting Oxygen Evolution Reaction Performance on NiFe-Based Catalysts Through d-Orbital Hybridization. *Nano Micro Lett.* **2025**, *17*, 11.
97. Wu, L.; Ning, M.; Xing, X.; et al. Boosting Oxygen Evolution Reaction of (Fe,Ni)OOH via Defect Engineering for Anion Exchange Membrane Water Electrolysis Under Industrial Conditions. *Adv. Mater.* **2023**, *35*, 2306097.
98. Wu, F.; Tian, F.; Li, M.; et al. Engineering Lattice Oxygen Regeneration of NiFe Layered Double Hydroxide Enhances Oxygen Evolution Catalysis Durability. *Angew. Chem.* **2025**, *64*, e202413250.
99. Zhang, R.; Ji, X.; Fan, Y.; et al. Local Coordination Engineering of NiFe-LDH Catalyst with Carboxylate and Sodium for Durable Seawater Oxygen Evolution. *Appl. Catal. B Environ. Energy* **2026**, *381*, 125850.
100. Luo, J.; Im, J.-H.; Mayer, M.T.; et al. Water Photolysis at 12.3% Efficiency via Perovskite Photovoltaics and Earth-Abundant Catalysts. *Science* **2014**, *345*, 1593–1596.
101. Anderson, G.C.; Pivovar, B.S.; Alia, S.M. Establishing Performance Baselines for the Oxygen Evolution Reaction in Alkaline Electrolytes. *J. Electrochem. Soc.* **2020**, *167*, 044503.
102. Anantharaj, S.; Kundu, S. Do the Evaluation Parameters Reflect Intrinsic Activity of Electrocatalysts in Electrochemical Water Splitting? *ACS Energy Lett.* **2019**, *4*, 1260–1264.
103. Anantharaj, S.; Karthik, P.E.; Noda, S. The Significance of Properly Reporting Turnover Frequency in Electrocatalysis Research. *Angew. Chem.* **2021**, *60*, 23051–23067.
104. Tsotridis, G.; Pilenga, A. EU *Harmonized Protocols for Testing of Low Temperature Water Electrolysis*; Publications Office of the European Union: Luxembourg, 2021.
105. Fang, Y.-H.; Liu, Z.-P. Tafel Kinetics of Electrocatalytic Reactions: From Experiment to First-Principles. *ACS Catal.* **2014**, *4*, 4364–4376.
106. Anantharaj, S.; Noda, S.; Driess, M.; et al. The Pitfalls of Using Potentiodynamic Polarization Curves for Tafel Analysis in Electrocatalytic Water Splitting. *ACS Energy Lett.* **2021**, *6*, 1607–1611.
107. Lyons, M.E.G.; Floquet, S. Mechanism of Oxygen Reactions at Porous Oxide Electrodes. Part 2—Oxygen Evolution at RuO_2, IrO_2 and $Ir_xRu_{1-x}O_2$ Electrodes in Aqueous Acid and Alkaline Solution. *Phys. Chem. Chem. Phys.* **2011**, *13*, 5314–5335.
108. Chen, J.; Ren, L.; Chen, X.; et al. Well-defined Nanostructures of High Entropy Alloys for Electrocatalysis. *Exploration* **2025**, *5*, 20230036.
109. Geiger, S.; Kasian, O.; Ledendecker, M.; et al. The Stability Number as a Metric for Electrocatalyst Stability Benchmarking. *Nat. Catal.* **2018**, *1*, 508–515.
110. Trotochaud, L.; Young, S.L.; Ranney, J.K.; et al. Nickel–Iron Oxyhydroxide Oxygen-Evolution Electrocatalysts: The Role of Intentional and Incidental Iron Incorporation. *J. Am. Chem. Soc.* **2014**, *136*, 6744–6753.
111. Corrigan, D.A. The Catalysis of the Oxygen Evolution Reaction by Iron Impurities in Thin Film Nickel Oxide Electrodes. *J. Electrochem. Soc.* **1987**, *134*, 377.
112. Wu, D.; Hu, L.; Liu, X.; et al. Time-Resolved Spectroscopy Uncovers Deprotonation-Induced Reconstruction in Oxygen-Evolution NiFe-Based (Oxy)Hydroxides. *Nat. Commun.* **2025**, *16*, 726.
113. Friebel, D.; Louie, M.W.; Bajdich, M.; et al. Identification of Highly Active Fe Sites in (Ni,Fe)OOH for Electrocatalytic Water Splitting. *J. Am. Chem. Soc.* **2015**, *137*, 1305–1313.
114. Wang, F.; Zou, P.; Zhang, Y.; et al. Activating Lattice Oxygen in High-Entropy LDH for Robust and Durable Water Oxidation. *Nat. Commun.* **2023**, *14*, 6019.
115. Zhao, S.; Tan, C.; He, C.T.; et al. Structural Transformation of Highly Active Metal–Organic Framework Electrocatalysts during the Oxygen Evolution Reaction. *Nat. Energy* **2020**, *5*, 881–890.

116. Wu, T.; Sun, S.; Song, J.; et al. Iron-Facilitated Dynamic Active-Site Generation on Spinel $CoAl_2O_4$ with Self-Termination of Surface Reconstruction for Water Oxidation. *Nat. Catal.* **2019**, *2*, 763–772.
117. Xiao, H.; Shin, H.; Goddard, W.A. Synergy between Fe and Ni in the Optimal Performance of (Ni,Fe)OOH Catalysts for the Oxygen Evolution Reaction. *Proc. Natl. Acad. Sci. USA* **2018**, *115*, 5872–5877.
118. Zheng, X.; Zhang, B.; De Luna, P.; et al. Theory-Driven Design of High-Valence Metal Sites for Water Oxidation Confirmed Using in Situ Soft *X*-Ray Absorption. *Nat. Chem.* **2018**, *10*, 149–154.
119. Li, Y.F.; Li, J.L.; Liu, Z.P. Structure and Catalysis of NiOOH: Recent Advances on Atomic Simulation. *J. Phys. Chem. C* **2021**, *125*, 27033–27045.
120. Zhang, H.; Zeng, Z.; Cheng, S.; et al. Recent Progress and Perspective on Lithium Metal Battery with Nickel-Rich Layered Oxide Cathode. *eScience*, **2024**, *4*, 100265.
121. Molina-Muriel, M.; Campagna Zignani, S.; Goberna-Ferrón, S.; et al. Efficient NiFe-Layered Double Hydroxide Electrocatalyst Synthesized via a Solvent-Free Mechanochemical Method for Oxygen Evolution Reaction. *ACS Omega* **2025**, *10*, 22671–22678.
122. Jin, L.; Sun, Y.; Zhou, X.; et al. One-Step Synthesis of Layered Double Hydroxides by a Solvent-Free Method. *ACS Sustain. Chem. Eng.* **2022**, *10*, 12955–12961.
123. Li, G.; Li, L.; Zhang, J.; et al. Enhance the Proportion of Fe^{3+} in NiFe-Layered Double Hydroxides by Utilizing Citric Acid to Improve the Efficiency and Durability of the Oxygen Evolution Reaction. *ChemSusChem* **2025**, *18*, e202401582.
124. Hayes, D.; Alia, S.; Pivovar, B.; et al. Targeted Synthesis, Characterization, and Electrochemical Analysis of Transition-Metal-Oxide Catalysts for the Oxygen Evolution Reaction. *Chem Catal.* **2024**, *4*, 100905.
125. Dai, J.; Zhang, Y.; Song, H.; et al. NiFe Layered-Double-Hydroxide Nanosheet Arrays Grown *in situ* on Ni Foam for Efficient Oxygen Evolution Reaction. *Int. J. Hydrogen Energy* **2024**, *87*, 130–137.
126. Liu, Z.Y.; Wang, Q.Y.; Hu, J.M. Introducing Carbon Dots to NiFe-LDH via a Mild Coprecipitation–Aging Method to Construct a Heterojunction for Effective Oxygen Evolution. *Catal. Sci. Technol.* **2024**, *14*, 110–118.
127. Li, Z.; Wei, P.; Wang, G. Recent Advances on Perovskite Electrocatalysts for Water Oxidation in Alkaline Medium. *Energy Fuels* **2022**, *36*, 11724–11744.
128. Chen, M.; Kitiphatpiboon, N.; Feng, C.; et al. Recent Progress in Transition-Metal-Oxide-Based Electrocatalysts for the Oxygen Evolution Reaction in Natural Seawater Splitting: A Critical Review. *eScience*, **2023**, *3*, 100111.
129. Wang, X.; Yu, M.; Feng, X. Electronic structure regulation of noble metal-free materials toward alkaline oxygen electrocatalysis. *eScience*, **2023**, *3*, 100141.
130. Li, D.; Park, E.J.; Zhu, W.; et al. Highly Quaternized Polystyrene Ionomers for High Performance Anion Exchange Membrane Water Electrolysers. *Nat. Energy* **2020**, *5*, 378–385.
131. Li, H.; Kraglund, M.R.; Reumert, A.K.; et al. Poly(Vinyl Benzyl Methylpyrrolidinium) Hydroxide Derived Anion Exchange Membranes for Water Electrolysis. *J. Mater. Chem. A* **2019**, *7*, 17914–17922.
132. Sankar, S.; Roby, S.; Kuroki, H.; et al. High-Performing Anion Exchange Membrane Water Electrolysis Using Self-Supported Metal Phosphide Anode Catalysts and an Ether-Free Aromatic Polyelectrolyte. *ACS Sustain. Chem. Eng.* **2023**, *11*, 854–865.
133. Park, Y.S.; Lee, J.; Jang, M.J.; et al. High-Performance Anion Exchange Membrane Alkaline Seawater Electrolysis. *J. Mater. Chem. A* **2021**, *9*, 9586–9592.
134. Zhang, J.; Zhao, S.; Chen, B.; et al. Sulfidation of $CoCuO_x$ Supported on Nickel Foam to Form a Heterostructure and Oxygen Vacancies for a High-Performance Anion-Exchange Membrane Water Electrolyzer. *ACS Appl. Mater. Interfaces* **2023**, *15*, 45756–45763.
135. Lee, J.; Jung, H.; Park, Y.S.; et al. High-Efficiency Anion-Exchange Membrane Water Electrolyzer Enabled by Ternary Layered Double Hydroxide Anode. *Small* **2021**, *17*, 2100639.
136. Choi, W.-S.; Jang, M.J.; Park, Y.S.; et al. Three-Dimensional Honeycomb-Like $Cu_{0.81}Co_{2.19}O_4$ Nanosheet Arrays Supported by Ni Foam and Their High Efficiency as Oxygen Evolution Electrodes. *ACS Appl. Mater. Interfaces* **2018**, *10*, 38663–38668.
137. Woo, J.; Han, S.; Yoon, J. Mn-Doped Sequentially Electrodeposited Co-Based Oxygen Evolution Catalyst for Efficient Anion Exchange Membrane Water Electrolysis. *ACS Appl. Mater. Interfaces* **2024**, *16*, 23288–23295.
138. Wang, H.; Sun, H.; Cao, S.; et al. Amorphous-Crystalline Interface Coupling Induced Highly Active Ultrathin NiFe Oxy-Hydroxide Design towards Accelerated Alkaline Oxygen Evolution. *J. Catal.* **2024**, *430*, 115354.
139. Park, Y.S.; Yang, J.; Lee, J.; et al. Superior Performance of Anion Exchange Membrane Water Electrolyzer: Ensemble of Producing Oxygen Vacancies and Controlling Mass Transfer Resistance. *Appl. Catal. B Environ.* **2020**, *278*, 119276.
140. Zhu, Y.; Chen, Y.; Feng, Y.; et al. Constructing Ru-O-TM Bridge in NiFe-LDH Enables High Current Hydrazine-assisted H_2 Production. *Adv. Mater.* **2024**, *36*, 2401694.
141. Li, Z.; Chen, G.; Gou, S.; et al. NiFe-LDH and PPy-Reinforced PVA Conductive Hydrogels for All-in-One High-Performance Supercapacitors. *J. Alloy Compd.* **2024**, *1009*, 176850.

142. Guo, L.; Xie, J.; Chen, S.; et al. Self-Supported Crystalline-Amorphous Composites of Metal Phosphate and NiS for High-Performance Water Electrolysis under Industrial Conditions. *Appl. Catal. B Environ.* **2024**, *340*, 123252.
143. Hu, Y.; Shen, T.; Wu, Z.; et al. Coordination Stabilization of Fe by Porphyrin-Intercalated NiFe-LDH Under Industrial-Level Alkaline Conditions for Long-Term Electrocatalytic Water Oxidation. *Adv. Funct. Mater.* **2025**, *35*, 2413533.
144. Inamdar, A.I.; Chavan, H.S.; Seok, J.H.; et al. Optimal Rule-of-Thumb Design of NiFeMo Layered Double Hydroxide Nanoflakes for Highly Efficient and Durable Overall Water-Splitting at Large Currents. *J. Mater. Chem. A* **2022**, *10*, 20497–20508.
145. Yang, Y.; Lie, W.H.; Unocic, R.R.; et al. Defect-Promoted Ni-Based Layer Double Hydroxides with Enhanced Deprotonation Capability for Efficient Biomass Electrooxidation. *Adv. Mater*. **2023**, *35*, 2305573.
146. Guo, W.; Yan, X.; Lu, Q.; et al. Mo-Modified NiFe LDH Nanoflower Anode Catalyst Synthesized via a Top-down Etching Method for Anion Exchange Membrane Water Electrolysis. *Int. J. Hydrogen Energy* **2025**, *145*, 237–249.
147. Ha, J.S.; Park, Y.; Jeong, J.-Y.; et al. Solar-Powered AEM Electrolyzer via PGM-Free (Oxy)Hydroxide Anode with Solar to Hydrogen Conversion Efficiency of 12.44%. *Adv. Sci*. **2024**, *11*, 2401782.
148. Zhao, T.; Wang, S.; Li, Y.; et al. Heterostructured V-Doped $Ni_2P/Ni_{12}P_5$ Electrocatalysts for Hydrogen Evolution in Anion Exchange Membrane Water Electrolyzers. *Small* **2022**, *18*, 2204758.
149. Han, Y.; Wang, J.; Liu, Y.; et al. Stability Challenges and Opportunities of NiFe-Based Electrocatalysts for Oxygen Evolution Reaction in Alkaline Media. *Carbon Neutraliz.* **2024**, *3*, 172–198.
150. He, L.; Zhou, Y.; Wang, M.; et al. Recent Progress on Stability of Layered Double Hydroxide-Based Catalysts for Oxygen Evolution Reaction. *Nanomaterials* **2024**, *14*,1533.
151. Iqbal, S.; Ehlers, J.C.; Hussain, I.; et al. Trends and Industrial Prospects of NiFe-Layered Double Hydroxide for the Oxygen Evolution Reaction. *Chem. Eng. J.* **2024**, *499*, 156219.
152. Xu, H.; Yao, B. Industrial Applications of Layered Double Hydroxide (LDH) Catalysts in High-Current Density Water Electrolysis. *Int. J. Hydrogen Energy* **2025**, *162*, 150714.